mathematics

MDPI

Article

Slope Stability Prediction Using *k*-NN-Based Optimum-Path Forest Approach

Leilei Liu, Guoyan Zhao and Weizhang Liang *

School of Resources and Safety Engineering, Central South University, Changsha 410083, China; leilei_liu@csu.edu.cn (L.L.)
* Correspondence: wzlian@csu.edu.cn

Abstract: Slope instability can lead to catastrophic consequences. However, predicting slope stability effectively is still challenging because of the complex mechanisms and multiple influencing factors. In recent years, machine learning (ML) has received great attention in slope stability prediction due to its strong nonlinear prediction ability. In this study, an optimum-path forest algorithm based on k-nearest neighbor ($OPF_{k\text{-}NN}$) was used to predict the stability of slopes. First, 404 historical slopes with failure risk were collected. Subsequently, the dataset was used to train and test the algorithm based on randomly divided training and test sets, respectively. The hyperparameter values were tuned by combining ten-fold cross-validation and grid search methods. Finally, the performance of the proposed approach was evaluated based on accuracy, F_1-score, area under the curve (AUC), and computational burden. In addition, the prediction results were compared with the other six ML algorithms. The results showed that the $OPF_{k\text{-}NN}$ algorithm had a better performance, and the values of accuracy, F_1-score, AUC, and computational burden were 0.901, 0.902, 0.901, and 0.957 s, respectively. Moreover, the failed slope cases can be accurately identified, which is highly critical in slope stability prediction. The slope angle had the most important influence on prediction results. Furthermore, the engineering application results showed that the overall predictive performance of the $OPF_{k\text{-}NN}$ model was consistent with the factor of safety value of engineering slopes. This study can provide valuable guidance for slope stability analysis and risk management.

Keywords: slope stability prediction; machine learning (ML); optimum-path forest (OPF); *k*-nearest neighbor (*k*-NN); hyperparameter tuning

MSC: 86-10

Citation: Liu, L.; Zhao, G.; Liang, W. Slope Stability Prediction Using *k*-NN-Based Optimum-Path Forest Approach. *Mathematics* **2023**, *11*, 3071. https://doi.org/10.3390/math11143071

Academic Editors: Danial Jahed Armaghani, Hadi Khabbaz, Manoj Khandelwal, Niaz Muhammad Shahani and Ramesh Murlidhar Bhatawdekar

Received: 15 June 2023
Revised: 10 July 2023
Accepted: 10 July 2023
Published: 12 July 2023

1. Introduction

Slope instability is a global geological problem, which is one of the three major geological problems in nature besides earthquakes and volcanoes. Many geotechnical projects, such as open-pit mining, mountain roads, tailings dams, and landfills, are seriously threatened by slope instability. A serious slope instability disaster can cause casualties, building damages, and huge economic losses. For example, on 20 December 2015, a catastrophic landslide occurred at the Hong'ao landfill in Shenzhen, China, resulting in 77 deaths, 33 buildings buried, and direct economic losses of more than 880 million RMB [1]. On the evening of 11 March 2017, a landslide at the Koshe landfill in Ethiopia's capital, Yah, caused 113 deaths and more than 80 people missing [2]. Due to heavy rainfall on 18 October 2020, a landslide occurred in Vietnam's Quang Tri province, claiming the lives of 22 soldiers [3]. Because of its serious consequences, predicting the risk of slope instability is crucial and plays a significant role in disaster prevention.

The prediction methods of slope stability can be classified into four categories. The first one is instrumental monitoring technology. Currently, many on-site monitoring techniques of slope deformation have been applied to monitor the early warning signs of

slope instability. For example, Zhang et al. [4] used distributed fiber optic strain sensors to monitor the shear displacement in the Three Gorges Reservoir region in China, and two potential circular sliding surfaces were successfully identified. Dixon et al. [5], Shiotani [6], and Codeglia et al. [7] adopted the acoustic emissions (AE) technology to monitor the signals generated by the fracture of soil and rock materials in the slope. By analyzing the relationship between AE characteristics and slope deformation, AE-based criteria were used to evaluate the long-term stability of slopes. In addition, some other techniques, such as remote sensing [8], terrestrial laser scanning [9], synthetic aperture radar [10], and time domain reflectometry [11], were applied to slope stability monitoring. These technologies have relatively high prediction accuracy because the precursor information of slope instability can be obtained directly, but the installation process is complicated, and the cost is high.

The second one is the theoretical analysis method. It is proposed from the view of mechanical mechanisms. Many theoretical and analytical approaches have been used to analyze slope stability, such as the limit equilibrium method (LEM) [12], the strength reduction method (SRM) [13], and the limit analysis method [14]. The factor of safety (FOS), calculated by the ratio of resisting force to driving force, is used to evaluate the stability of the slope. When the value of FOS is larger than 1, the slope is stable; otherwise, it is unstable [15]. Faramarzi et al. [16] employed LEM to calculate the FOS and analyzed the rock slope stability of the Chamshir dam pit. Liu [17] adopted the SRM to obtain the FOS of the established slope model. Mbarka et al. [18] combined the Monte Carlo approach, LEM, and SRM for the reliability analysis of homogeneous slopes with circular-type failure. Although the theoretical and analytical methods are simple, they are unsuitable for slopes with complex conditions due to the simplified formulas and assumptions.

The third one is the numerical simulation technique. With the rapid development of numerical simulation methods, finite element method (FEM) [19], boundary element method [20], discrete element method [21], numerical manifold method [22], and other methods have been widely used in slope stability analysis. Sun et al. [23] simulate the progressive failure process of jointed rock slopes based on the combined finite-discrete element method. Ma et al. [24] analyzed the slope stability under a complex stress state with saturated and unsaturated seepage using the fast Lagrangian analysis of continua. Wei et al. [25] investigated the kinetic features of slope instability based on particle flow code. Haghnejad et al. [26] analyzed the effect of blast-induced vibration on slope stability using dynamic pressure in three dimensions distinct element codes. Song et al. [27] adopted an improved smoothed-particle hydrodynamics method to calculate the slope safety factor. Zhang et al. [28] adopted a realistic failure process analysis to evaluate the stability and investigated the failure mode of the high rock slope during excavations. In addition, some researchers have integrated numerical simulation and mathematical methods to analyze the slope stability. For example, Dyson and Tolooiyan [29] adopted FEM and Monte Carlo to determine the FOS and damage probability of slopes. Although the numerical simulation methods are convenient to operate, the accuracy strongly depends on constitutive models and mechanical parameters [30].

The fourth one is the machine learning (ML) algorithm. With the accumulation of slope cases, some researchers attempted to develop slope stability prediction models using ML algorithms. There are two types of predicted outputs: FOS and stability status. Lu and Rosenbaum [31] adopted an artificial neural network to estimate the FOS and SS on 46 slope cases collected by Sah et al. [32]. Based on the same database, Samui [33] and Yang et al. [34] used a support vector machine (SVM) and genetic programming to determine FOS, respectively. Amirkiyaei and Ghasemi [35] constructed two tree-based models to assess circular-type failure slopes based on 87 cases. Zhou et al. [36] collected 221 slope cases and employed the gradient-boosting machine to predict the SS. Wang et al. [37] hybridized a genetic algorithm with a multi-layer perceptron to predict FOS using 630 cases. In addition, several researchers performed a comparative analysis of multiple ML algorithms. Hoang and Tien Bui [38] carried out a comparative study of SS prediction using a ra-

dial basis function neural network, an extreme learning machine, and least squares SVM. Mahmoodzadeh et al. [39] adopted Gaussian process regression, support vector regression, decision trees (DT), long-short-term memory, deep neural networks, and *k*-nearest neighbors (*k*-NN) to determine FOS. All the above ML algorithms performed well on slope stability prediction. However, a large number of slope stability cases are required to improve its credibility.

Compared with other approaches, ML algorithms can obtain reliable prediction results by establishing the nonlinear relationship between input and output. It is a promising method for predicting slope stability. But to date, there is no one ML algorithm that can be applied to all slope engineering conditions under the consensus of the geotechnical industry. Accordingly, it is meaningful to investigate more robust ML algorithms to achieve better prediction results. Recently, the optimum-path forest (OPF) algorithm has been successfully applied in many fields, such as face recognition [40], Parkinson's disease identification [41], laryngeal cancer pathology detection [42], land use classification [43], and network intrusion detection [44]. However, the OPF algorithm is susceptible to outliers. In response to this deficiency, Papa et al. [45] proposed the OPF algorithm based on *k*-NN ($OPF_{k\text{-}NN}$), and the discriminative performance of the OPF model was improved. In combination with the *k*-NN algorithm, the $OPF_{k\text{-}NN}$ algorithm can provide better performance for classification tasks by leveraging the topological properties of the data [46]. Compared to other classification algorithms, the $OPF_{k\text{-}NN}$ algorithm has several advantages, including (1) it is free of hyperparameters, (2) it does not assume separability of the feature space, (3) it has a unique feature selection and classification mechanism that can effectively handle the high-dimensional and nonlinear data with outliers, (4) and its training step is usually much faster than traditional ML approaches.

Considering that the $OPF_{k\text{-}NN}$ has great predictive performance and has not yet been employed to predict the stability of slopes, this study aims to investigate the feasibility of $OPF_{k\text{-}NN}$ for predicting slope stability. In addition, a comparison against OPF, radial basis function support vector machine (RBF-SVM), random forest (RF), DT, *k*-NN, and logistic regression (LR) classifiers is performed.

2. Methodology

2.1. k-NN Based OPF Classifier

The OPF is a graph-based classifier [47,48]. Its classification principle is to denote the training samples as nodes and connect them by path. Then, the optimal path tree (OPT) is constructed by executing the shortest path algorithm on the graph. Finally, the test sample is mapped onto the OPT, and its class is determined. Figure 1 shows the schematic diagram of the OPF-based classifiers. The nodes with different colors in the set S represent different classes, and the nodes outside the set S are the samples to be classified. A series of adjacent nodes are defined as path π. Among all paths, the one with the maximum path-cost function $f(\pi_t)$ is called OPT, and all OPTs constitute OPF. There are three different classes in Figure 1; the blue sample s is the root node of the OPT where sample t is located, so sample t is classified as blue.

The $OPF_{k\text{-}NN}$ is a variant of the OPF algorithm, and the main difference between them is the adjacency of the samples in the training set. The latter is to construct a complete graph, while the former is to construct a *k*-NN graph [45]. The $OPF_{k\text{-}NN}$ algorithm is divided into training and classification phases.

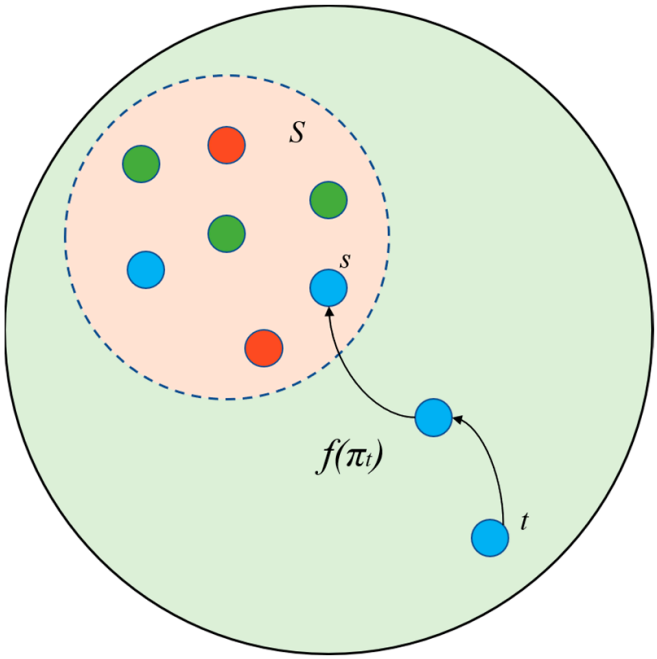

Figure 1. Schematic diagram of OPF-based classifiers [49].

2.1.1. Training Phase

The first step is to construct a k-NN graph G_k based on the training set Z_1. The sample s is weighed by a probability density function $\rho(s)$:

$$\rho(s) = \frac{1}{\sqrt{2\pi\sigma^2}|G_k^*(s)|} \sum_{\forall t \in G_k^*(s)} \exp\left(\frac{-d^2(s,t)}{2\sigma^2}\right), \tag{1}$$

where $\sigma = \frac{d_f}{3}$, d_f is the maximum arc weight in G_k, and $d(s, t)$ is the distance between sample s and sample t.

The second step is to calculate the path cost function $f_{\min}$, which is defined as:

$$\begin{aligned} f_{\min}(\langle t \rangle) &= \begin{cases} \rho(t) & \text{if } t \in S \\ \rho(t) - 1 & \text{otherwise} \end{cases}, \\ f_{\min}(\pi_s \cdot \langle s,t \rangle) &= \min\{f_{\min}(\pi_s), \rho(t)\} \end{aligned} \tag{2}$$

According to the method proposed by Papa et al. [50], the k value of k-NN is determined by maximizing the accuracy of the training set in the range $[1, k_{\max}]$. The value of $k_{\max}$ defaults to 5. After determining the value of k, the algorithm is applied to retrain the classifier. The function $f_{\min}$ is replaced by $f'_{\min}$, which is defined as:

$$\begin{aligned} f'_{\min}(\langle t \rangle) &= \begin{cases} \rho(t) & \text{if } t \in S \\ \rho(t) - 1 & \text{otherwise} \end{cases} \\ f'_{\min}(\pi_s \cdot \langle s,t \rangle) &= \begin{cases} -\infty & \text{if } \lambda(t) \neq \lambda(s) \\ \min\{f'_{\min}(\pi_s), \rho(t)\} & \text{otherwise} \end{cases} \end{aligned}. \tag{3}$$

Figure 2 is the schematic diagram of the training phase, where Figure 2a indicates the k-NN graph generated from the training set, Figure 2b represents the minimum spanning tree calculated by the k-NN graph, Figure 2c denotes the two samples of different colors labeled as prototype samples (marked by black dashed circles), and Figure 2d signifies the $\text{OPF}_{k\text{-NN}}$ classifier composed by all the OPTs. The red squares and green circles represent different classes, respectively.

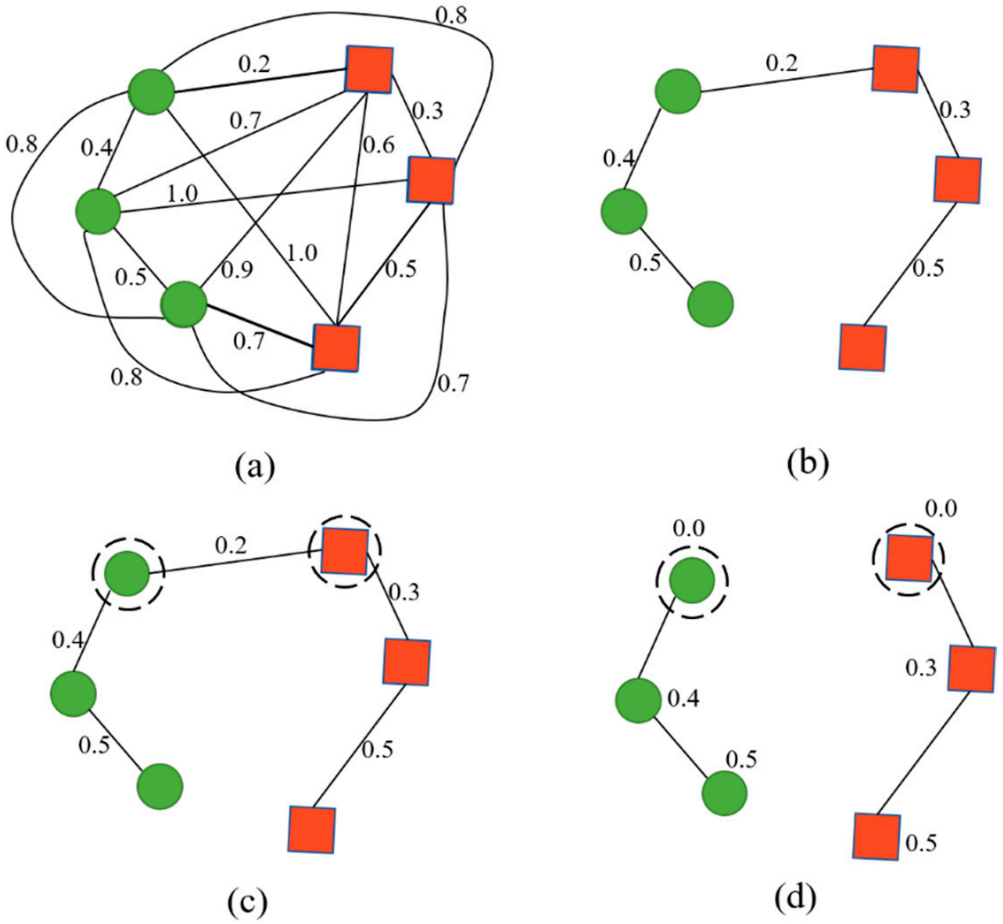

Figure 2. Schematic diagram of the training phase [50], (**a**) a two-class ("green circles" and "red squares") complete graph, (**b**) minimum spanning tree (MST), (**c**) labeled prototypes (marked by black dashed circles), (**d**) optimal path forest.

2.1.2. Classification Phase

After training the $OPF_{k\text{-NN}}$ classifier, the sample t in the test set Z_2 is classified. The k-NN is first calculated from Z_1 to a testing sample t. Then, it is verified which sample $s \in Z_1$ satisfies the equation below:

$$V(t) = \max\{\min[V(s), \rho(t)]\} \forall s \in Z_1 \tag{4}$$

Figure 3 indicates the classification process of $OPF_{k\text{-NN}}$. The blue triangle is the sample to be classified. Figure 3a shows that the blue triangle is connected to the k-nearest training samples in the generated OPF, and Figure 3b illustrates that the triangle is conquered by the samples of the red squares class and labeled as red.

2.2. Proposed Approach

Figure 4 depicts the flowchart of the proposed approach. First, due to the different units of indicators and the diversity of data distribution, the raw data is pre-processed. The dataset is standardized using a Gaussian distribution with zero mean and unit standard deviation. Subsequently, 80% of samples are used for training, and the remaining 20% are adopted for testing [51,52]. For the k-NN, RBF-SVM, RF, DT, and LR algorithms, the grid search and ten-fold cross-validation (CV) methods are used to select the optimal hyperparameters. Finally, the test set is predicted, and the optimal classifier is determined according to the evaluation metrics.

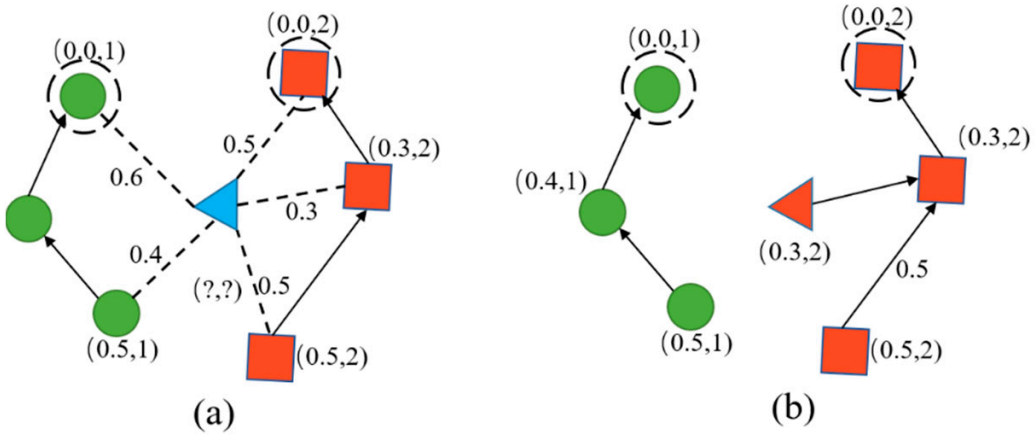

Figure 3. Schematic diagram of classification phase [50], (**a**) the sample to be classified (blue triangle) is connected to all training nodes in the generated optimal path forest, and the connection strength $f$max is calculated for each path, (**b**) the triangle is conquered by "red squares" class samples and classified as "red".

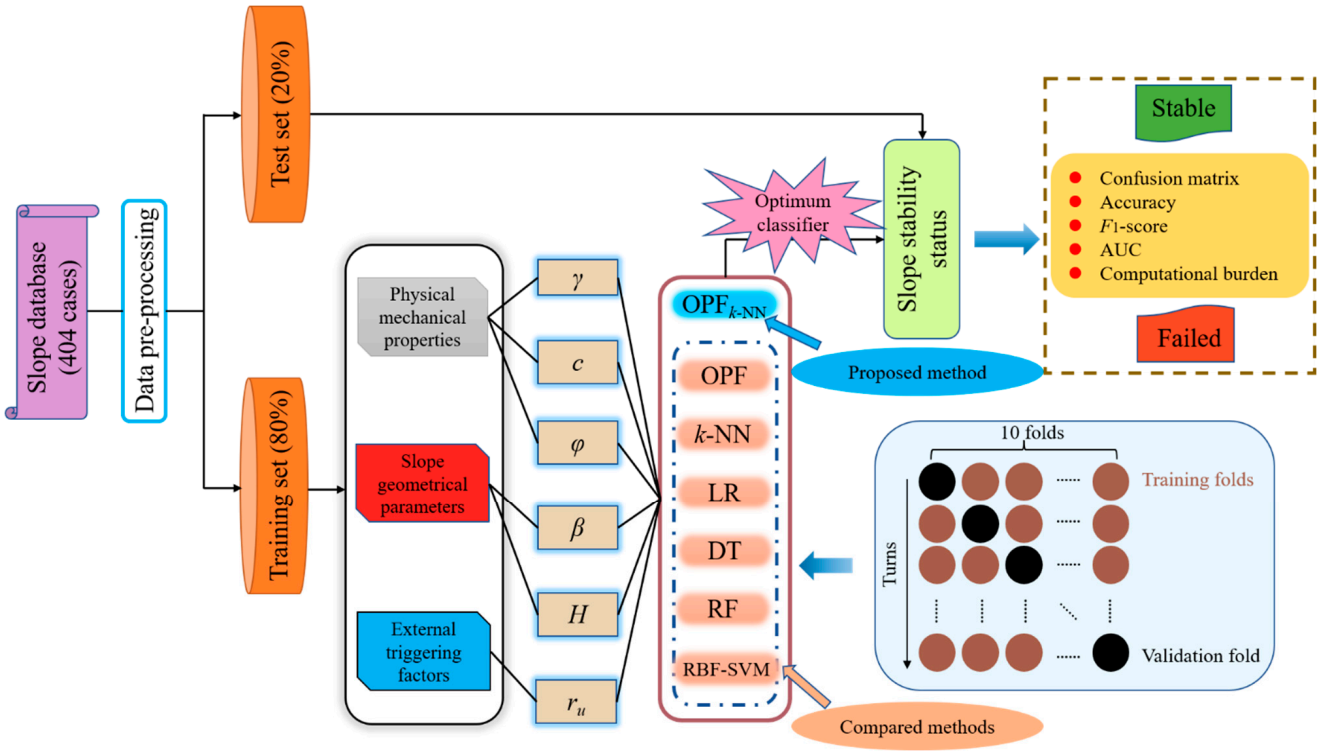

Figure 4. Flowchart of the proposed approach.

The OPF$_{k\text{-NN}}$ and OPF are implemented based on the Python library "opfython" [53], and the k-NN, RBF-SVM, RF, DT, and LR are conducted on the Python library "scikit-learn" [54]. All experiments are conducted using a Windows1064 bits computer with 8Gb of RAM running an Intel® Core™ i7-9700F CPU @ 3.00 GHz × 2.

If the predictive performance of our proposed approach is acceptable, it can be used for engineering applications in several ways. For example, it can be integrated into slope monitoring systems to provide real-time alerts for potential instability. The model can also be used to evaluate slope stability during the design phase of construction projects to ensure the safety and stability of the slope. Additionally, the model can be applied to slope stability analysis and risk management, which can be used by geotechnical engineers in various projects related to slope instability.

2.3. Performance Evaluation Metrics

In this study, several metrics are used to evaluate the performance of classifiers and figure out the optimal classifier for slope stability prediction [30,55].

A confusion matrix, which can also be called a likelihood table or error matrix, is used to visually represent whether the performance is ideal or not. Table 1 shows the confusion matrix for the slope-stability prediction, where true positive (*TP*) means the number of stable cases predicted correctly, false positive (*FP*) means the number of stable cases predicted incorrectly, true negative (*TN*) means the number of failed cases predicted correctly, and false negative (*FN*) means the number of failed cases predicted incorrectly. According to Table 1, true negative rate ($TN/(TN + FP)$) and false positive rate ($FP/(FP + TN)$) can be defined.

Table 1. Confusion matrix for slope stability prediction.

Actual Condition	**Predicted Condition**	
	Stable	**Failed**
Stable	True positive	False negative
Failed	False positive	True negative

Accuracy indicates the ratio of the cases correctly predicted to the total cases, which can be calculated by: $accuracy = (TP + TN)/(TP + TN + FP + FN)$.

F_1-score indicates the harmonic mean of precision and recall, which can be calculated by: $F_1\text{-score} = 2precision \cdot recall/(precision + recall)$, where $precision = TP/(TP + FP)$, $recall = TP/(TP + FN)$.

The area under the curve (AUC) is defined as the area under the receiver operating characteristic (ROC) curve, which is commonly used to evaluate the performance of classifiers. Bradley [56] proposed classification criteria of AUC as follows: not discriminating (0.5–0.6), poor (0.6–0.7), fair (0.7–0.8), good (0.8–0.9), and excellent (0.9–1).

Computational burden is used to evaluate the computational efficiency of algorithms. The mean and standard deviation of computation time are used as the evaluation metrics in this study.

2.4. Hyperparameter Tuning

In general, the performance of most ML algorithms is highly dependent on the hyperparameters. There are several hyperparameter tuning methods, such as manual search, grid search, random search, Bayesian optimization, gradient-based optimization, and evolutionary optimization [57]. In this study, the grid search algorithm is combined with the *k*-fold CV method to select the optimal hyperparameters.

The grid search algorithm is to grid the hyperparameters in a fixed range in equal steps, compare all hyperparameter combinations exhaustively, and then select the optimal hyperparameters. To avoid the risk of overfitting or selection bias in the model, the *k*-fold CV method is used in the hyperparameter tuning process, illustrated in Figure 5. The original training set is randomly split into k folds, of which $k - 1$ folds are used as the training sub-set, and the remaining fold is used as the validation set in turn. Then, the average accuracy of k rounds is calculated to evaluate the performance and determine the optimal hyperparameters [58]. In this study, k was selected as 10 after considering the calculation time and variance [59].

Figure 5. Flowchart of *k*-fold CV.

3. Data Collection

3.1. Dataset Description

The failure surfaces of the slopes are prone to occur near the potential slip surface. Because of the excavation at the foot of the slope or water seepage at the top of the slope, the shear stress on the potential slip surface exceeds the shear strength, causing the local slope instability, as shown in Figure 6. A large number of engineering cases and theoretical analyses indicate that there are three main aspects that affect slope stability: the physical–mechanical properties of the potential slip surface, the basic geometrical parameters, and the external triggering factors. [12,18,60–62]. Considering the independent correlation between indicators and the easy availability of indicator values, six indicators were selected in this study, including the unit weight (γ), the cohesion (c), the internal friction angle (φ), the slope angle (β), the slope height (H), and the pore pressure ratio (r_u). The detailed descriptions of these indicators are displayed in Table 2.

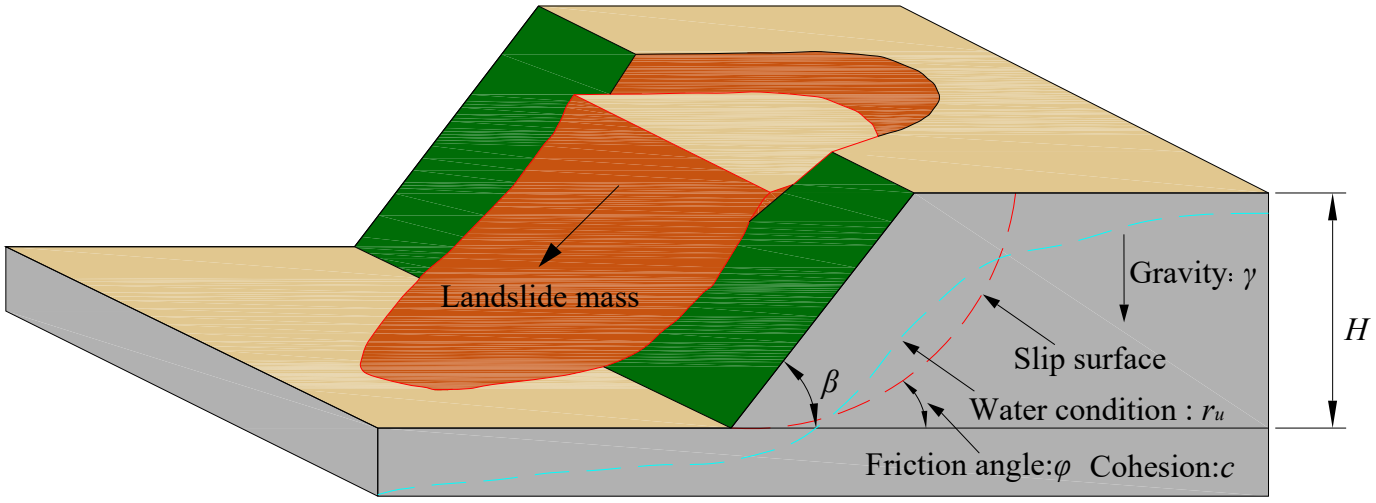

Figure 6. The 3D schematic diagram of slope failure.

Table 2. Descriptions of input indicators.

Indicator	Description	Measurement Method
γ (kN/m^3)	It indicates the weight of soil/rock per unit volume.	It can be measured by performing the standard mass volume method, mercury displacement method, or gravimeter method in the laboratory.
c (kPa)	It indicates the attraction between molecules on the surface of adjacent material particles within the soil/rock.	It can be determined by performing direct shear tests and triaxial compression tests in the laboratory.
φ (°)	It indicates a measure of the ability of a unit of soil/rock to withstand shear stress.	It can be determined by performing direct shear tests and triaxial compression tests in the laboratory.
β (°)	It indicates the angle between the slope plane and the slope bottom.	It can be measured in the field by an inclinometer.
H (m)	It indicates the vertical distance from the slope bottom to the slope top.	It can be measured in the field using a surveying instrument such as a total station.
r_u	It is defined as the ratio of the pore pressure and normal stress at a certain point within a slope.	It can be measured by installing pore water piezometers on-site or by performing immersion tests or infiltration tests in the laboratory.

In this study, a database of 404 slopes with failure risk from various countries was collected (available in "Appendix A") [32,36,57,63–72]. There are two statuses of slope stability: stable (207 cases) and failed (197 cases). Among them, most of the failed slopes were circular-type failures. The distribution of slope SS on the overall dataset is given in Figure 7, and the statistical values of data samples are illustrated in Table 3.

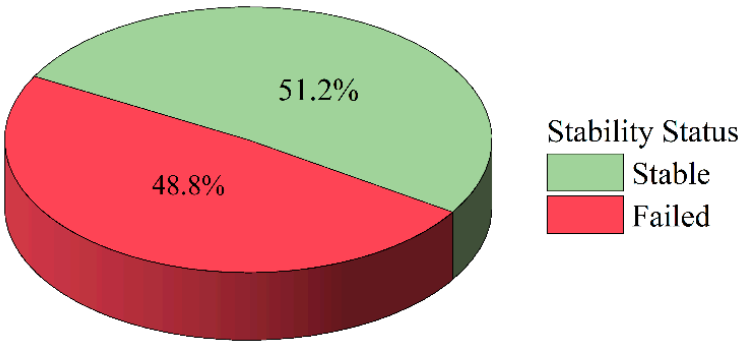

Figure 7. Distribution of slope stability status.

Table 3. Statistical values of slope stability dataset.

Value Type	γ (kN/m^3)	c (kPa)	φ (°)	β (°)	H (m)	r_u
Minimum	10.06	0	0	4.24	3.45	0
Median	21.38	29.7	28.27	34.03	51	0.2
Maximum	31.3	300	57.36	59.35	565	0.75
Mean	21.69	39.38	27.74	34.19	84.26	0.18
Standard	3.84	40.54	9.63	10.86	94.97	0.17

3.2. Dataset Analysis

The violin plots of six indicators are shown in Figure 8. They were a combination of box plots and density plots and indicated the overall distribution of the dataset. For each violin plot, the white dot in the center was the median of the samples, the top and bottom of the thick black line represented the third and first quartile of the samples, and the top and bottom of the thin black line indicated the upper and lower adjacent value. From Figure 8, it can be seen that the distribution of γ, φ, β was relatively balanced, and the medians were basically in the middle of the violin plots. While for c, H, r_u, there were some individual outliers.

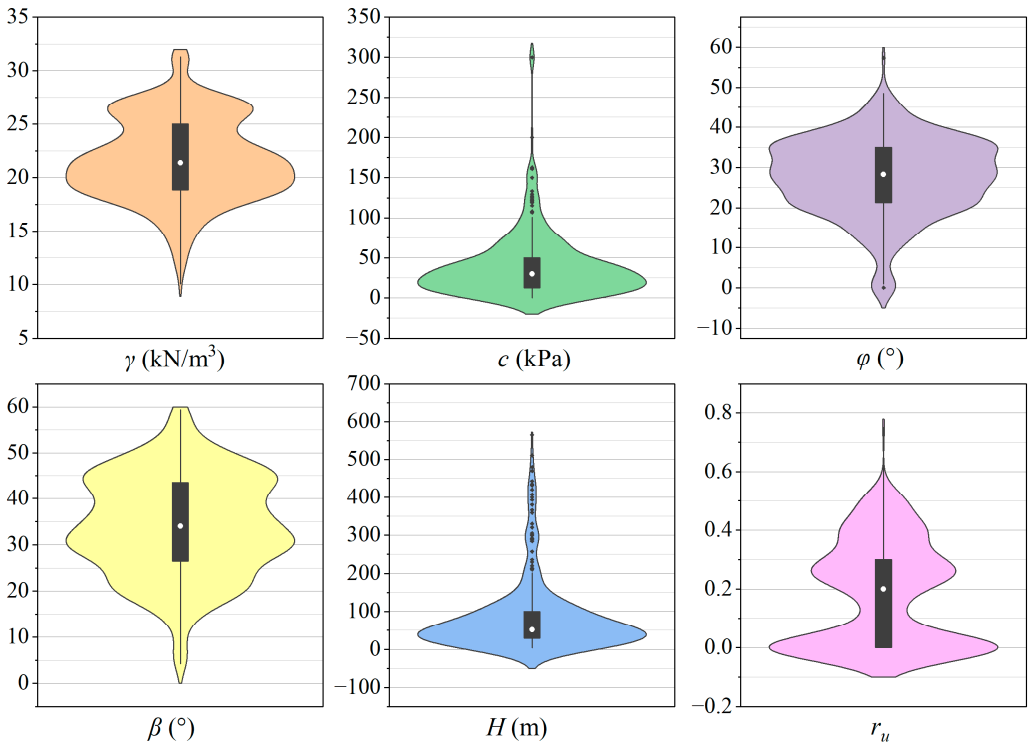

Figure 8. Violin plots of the dataset.

The heatmap of the Pearson correlation coefficient between each indicator is shown in Figure 9. According to Figure 9, all correlation coefficients were less than 0.5, and the highest correlation was only 0.41, which indicated that the correlation between indicators was poor. Therefore, all indicators were relatively independent and important for predicting slope stability.

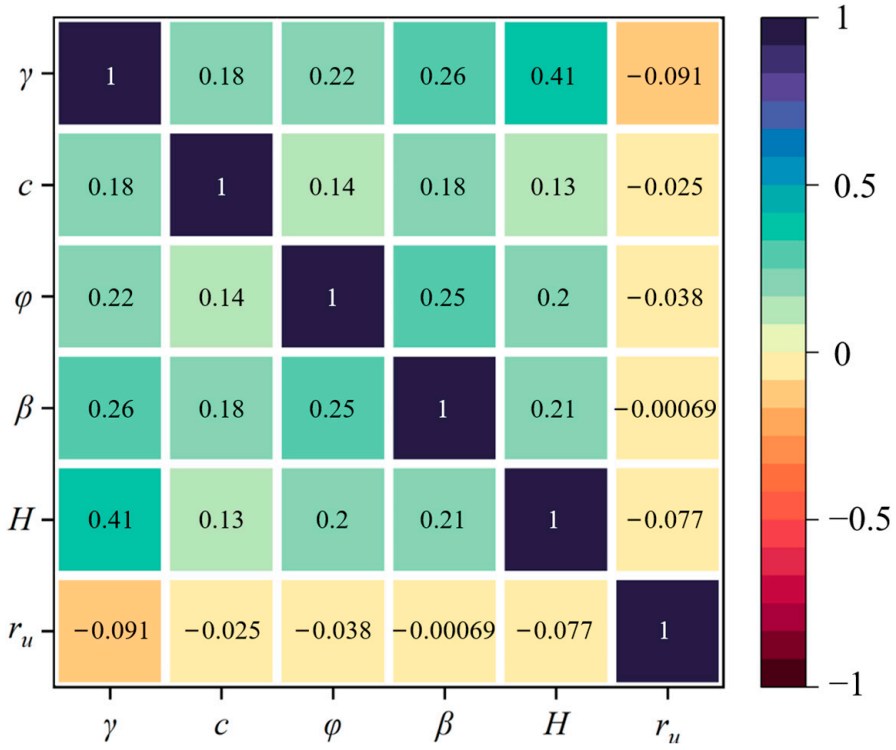

Figure 9. Correlation matrix of six indicators.

To visualize the distribution of the dataset, the correlation pair plots of the two slope SS were displayed in Figure 10. The distribution plots of these six indicators were shown on the diagonal line, and the correlation scatter plots between indicators were shown on the non-diagonal line. It can be seen that the differences in the distribution of indicators for both slope statuses were slight, and there was no apparent correlation among the indicators. Therefore, it was difficult to classify the slope SS only using one indicator, and the effect of all indicators should be incorporated for better accuracy.

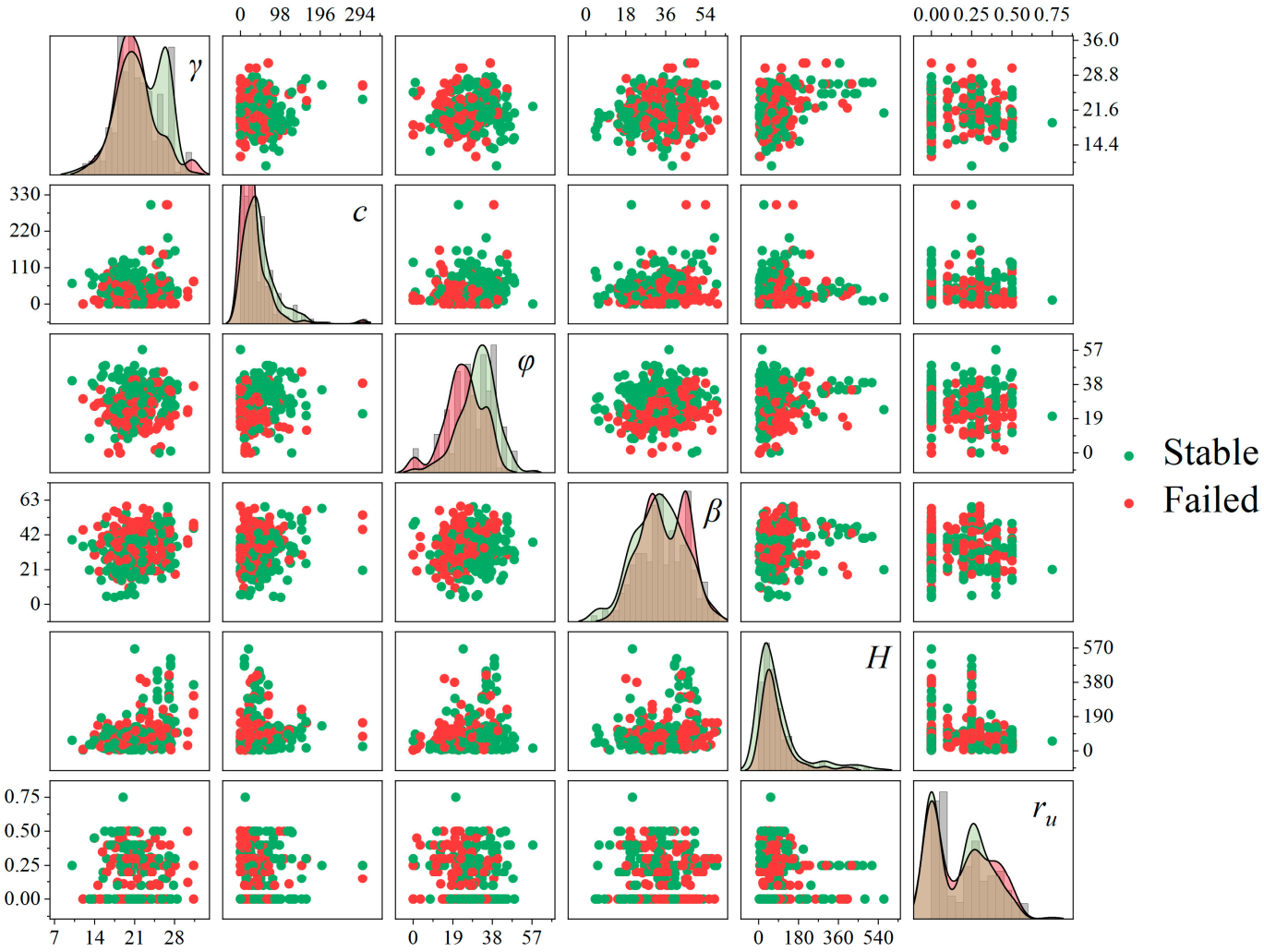

Figure 10. Correlation pair plots of six indicators.

4. Results and Analysis

4.1. Results of Hyperparameters Tuning

The average accuracy of ten-fold CV corresponding to different hyperparameters for *k*-NN, LR, DT, RF, and RBF-SVM algorithms is shown in Figure 11. According to Figure 11, the overall performance can be observed. With the increase of hyperparameter values, the average accuracy of LR decreased, but the other models had several peaks. Compared with other models, the results of RF were more stable. Based on the best average accuracy of ten-fold CV, the optimal hyperparameter values were determined. The scope, interval, and final optimization results of hyperparameter values are indicated in Table 4.

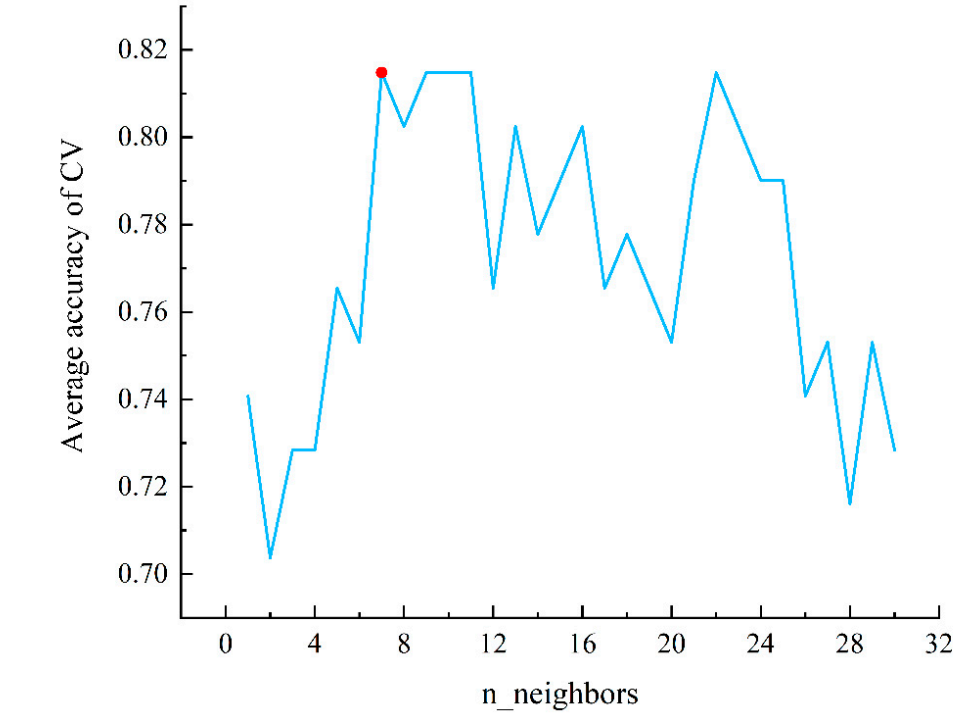

(**a**)

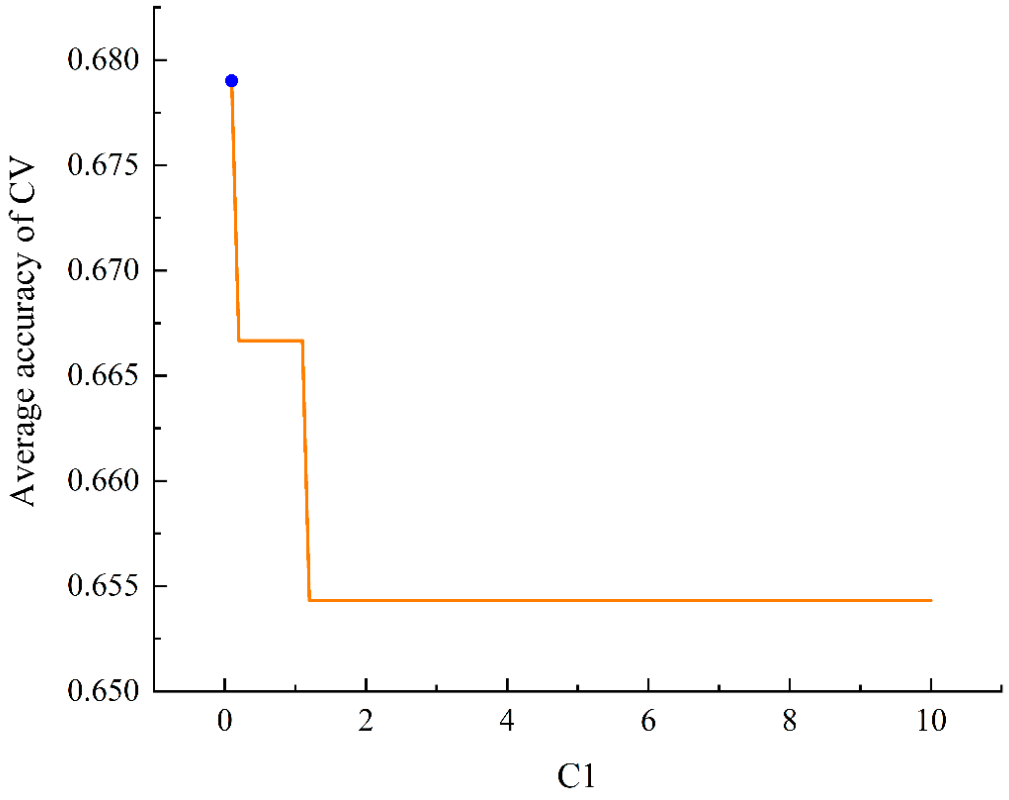

(**b**)

Figure 11. *Cont.*

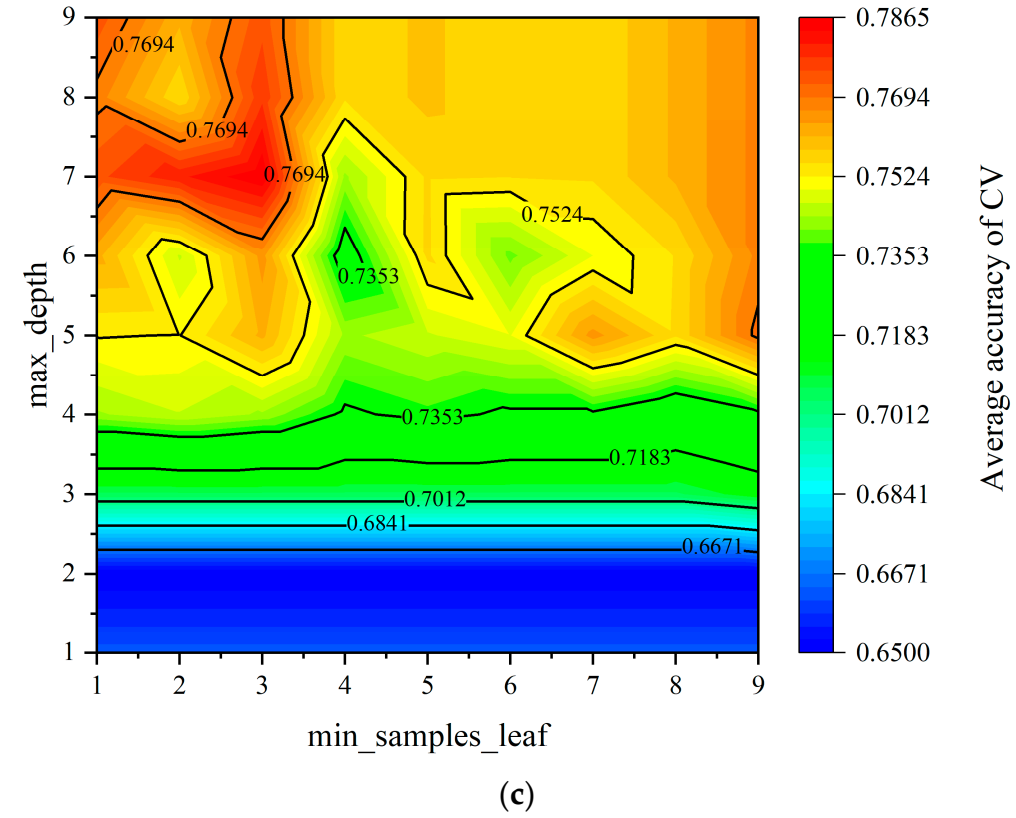

(**c**)

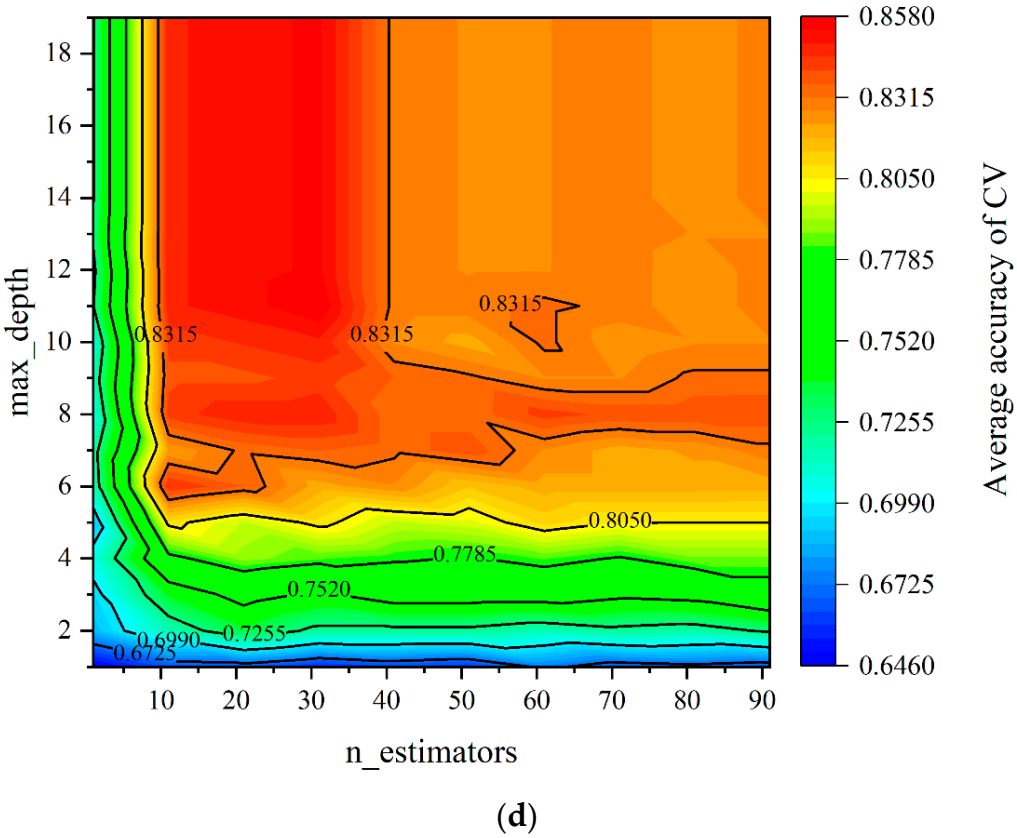

(**d**)

Figure 11. *Cont.*

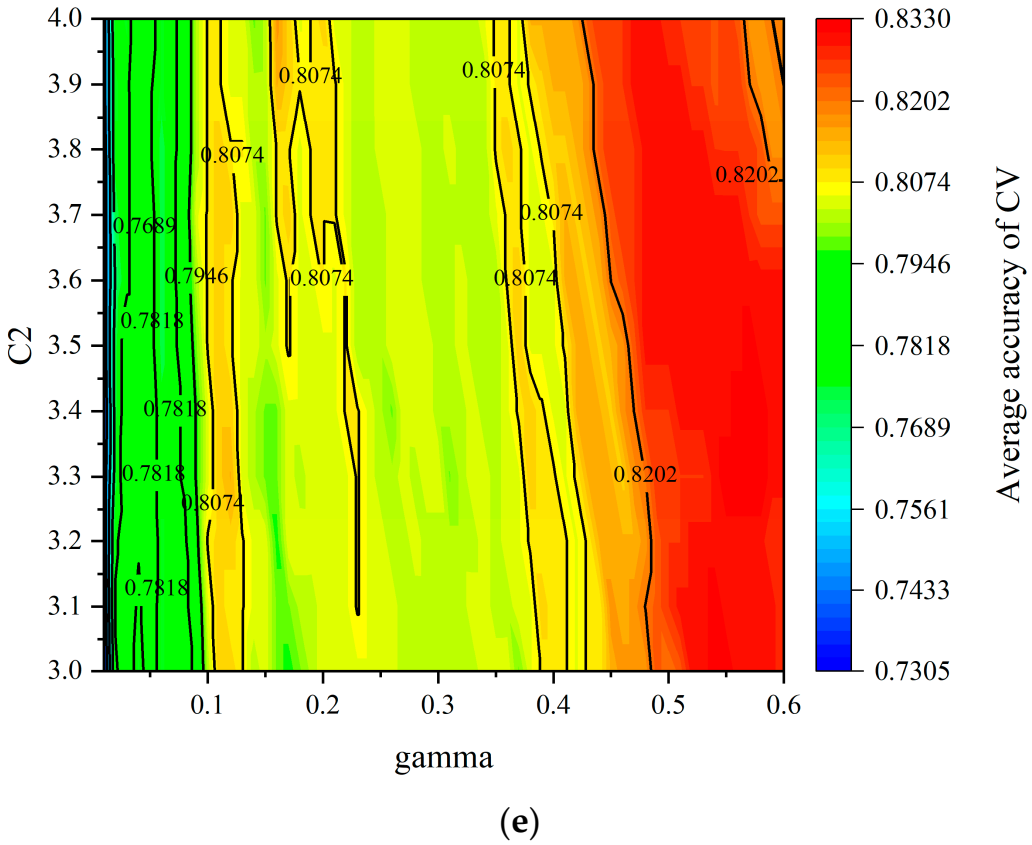

Figure 11. Grid search of hyperparameters tuning: (**a**) *k*-NN, (**b**) LR, (**c**) DT, (**d**) RF, and (**e**) RBF-SVM.

Table 4. Results of hyperparameters tuning.

ML Algorithms	Hyperparameters	Scope of Values	Interval of Values	Optimal Values
k-NN	n_neighbors	(1, 31)	1	7
LR	Inverse of regularization strength C1	(0.1, 10)	0.1	0.1
DT	max_depth	(1, 10)	1	7
	min_samples_leaf	(1, 10)	1	3
RF	n_estimators	(1, 101)	10	31
	max_depth	(1, 20)	1	11
RBF-SVM	gamma	(0.01, 0.6)	0.01	0.55
	Penalty coefficient C2	(3, 4)	0.1	3.3

4.2. Models Comparison and Evaluation

After the hyperparameters were tuned, these seven ML algorithms were used to predict slope stability based on the test set. The confusion matrix, accuracy, and F_1-score were calculated to compare the performance of each algorithm, which were illustrated in Table 5. It can be observed that $OPF_{k\text{-NN}}$ performed best with the highest accuracy of 0.901, followed by OPF, RF, *k*-NN, RBF-SVM, and DT with an accuracy of 0.876, 0.827, 0.815, 0.802, and 0.765, respectively. LR performed worst with an accuracy of 0.679. Furthermore, the rank was the same when using the F_1-score. Therefore, based on the overall prediction performance, the rank was $OPF_{k\text{-NN}}$ > OPF > RF > *k*-NN > RBF-SVM > DT > LR.

The ROC curves and AUC values of these seven classifiers are presented in Figure 12. It can be seen that the ROC curve of the $OPF_{k\text{-NN}}$ classifier was closer to the left and upper axes than others, indicating better performance. The AUC values of $OPF_{k\text{-NN}}$, RBF-SVM, RF, OPF, *k*-NN, DT, and LR were 0.895, 0.885, 0.876, 0.870, 0.783, and 0.720, respectively. According to the AUC classification criterion mentioned in Section 2.3, only $OPF_{k\text{-NN}}$

performed excellently, RBF-SVM, RF, OPF, and *k*-NN performed well, while DT and LR performed fair.

Table 5. Confusion matrix, accuracy, and F_1-score of the classifiers.

Classifiers	Actual Condition	Predicted Condition		Accuracy	F_1-Score
		Stable	Failed		
$OPF_{k\text{-NN}}$	Stable	37	4	0.901	0.902
	Failed	4	36		
OPF	Stable	38	3	0.876	0.884
	Failed	7	33		
RF	Stable	37	7	0.827	0.841
	Failed	7	30		
k-NN	Stable	36	8	0.815	0.828
	Failed	7	30		
RBF-SVM	Stable	35	9	0.802	0.814
	Failed	7	30		
DT	Stable	33	11	0.765	0.776
	Failed	8	29		
LR	Stable	28	16	0.679	0.683
	Failed	10	27		

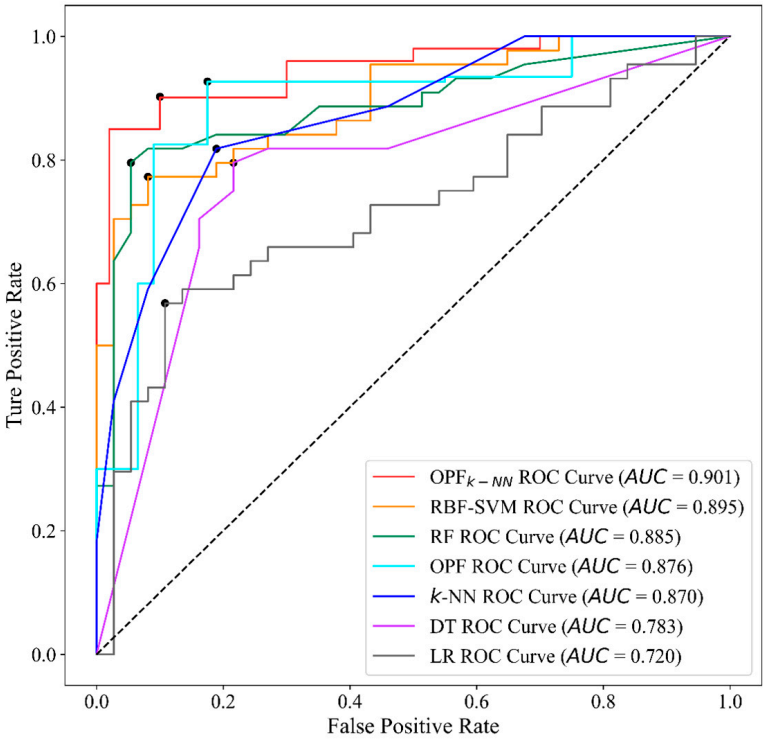

Figure 12. ROC curves and AUC of seven classifiers.

The average computation time for each classifier during the training and testing phases over 20 runs was calculated, as listed in Table 6. The results were presented in the following format: $x \pm y$, where x and y indicated the average time and standard deviation, respectively—noted that the values in bold indicated the minimum time consumed. It can be observed that the *k*-NN took the least time in the training phase, followed by LR, OPF, $OPF_{k\text{-NN}}$, RBF-SVM, and RF. In the testing phase, the time consumed by each classifier was not significantly different, and the difference between the maximum and minimum values was less than 0.2 s. For the total time, the rank was *k*-NN > LR > OPF > $OPF_{k\text{-NN}}$ > DT > RBF-SVM > RF. The total computation time of the $OPF_{k\text{-NN}}$ classifier was less than 1 s.

Table 6. Average computation time of classifiers over 20 runs.

Time	$OPF_{k\text{-}NN}$	OPF	RF	RBF-SVM	DT	LR	*k*-NN
Train	0.915 ± 0.027	0.322 ± 0.034	117.751 ± 1.163	82.326 ± 1.149	2.162 ± 0.067	0.402 ± 0.035	**0.187 ± 0.011**
Test	0.042 ± 0.002	0.097 ± 0.004	0.055 ± 0.003	0.171 ± 0.005	**0.008 ± 0.001**	**0.008 ± 0.001**	0.011 ± 0.002
Total	0.957 ± 0.026	0.419 ± 0.033	117.806 ± 1.164	82.497 ± 1.149	2.170 ± 0.067	0.410 ± 0.036	**0.198 ± 0.011**

4.3. Relative Importance of Indicators

The relative importance of indicators was significant for the design of support structures in slope engineering. In this study, the relative importance of each indicator was calculated by combining the $OPF_{k\text{-}NN}$ model with the permutation feature importance technique [73]. The permutation feature importance is a model inspection technique available in the Python library "scikit-learn" [54]. Values of indicators were shuffled in turn within the test set, the slope stability prediction results were generated by the $OPF_{k\text{-}NN}$ model, and the accuracy changes were recorded. Then, the prediction accuracy changes of indicators were ranked, and the relative importance was derived. As shown in Figure 13, the slope angle was the most important indicator with an importance value of 30.5%, followed by internal friction angle (22%), cohesion (19.7%), unit weight (12.3%), slope height (7.93%), and pore pressure ratio (7.63%).

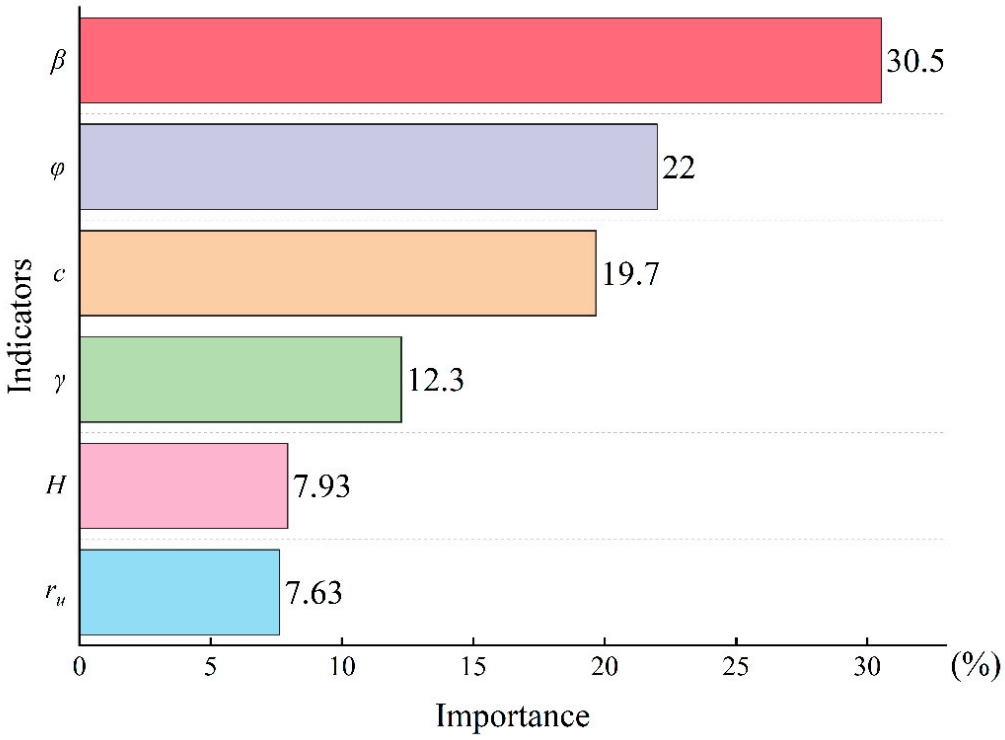

Figure 13. Relative importance of indicators.

5. Discussions

The prediction of failed cases is particularly important, which may lead to the development of slope instability if predicted incorrectly [74]. Therefore, the false positive rate and true negative rate were presented together in Figure 14. It can be seen that the false positive rate and true negative rate of RBF-SVM, *k*-NN, and RF were the same, and the $OPF_{k\text{-}NN}$ had the largest true negative rate and the lowest false positive rate. From this view, the $OPF_{k\text{-}NN}$ classifier performed better. The reason is that the $OPF_{k\text{-}NN}$ algorithm can effectively process high-dimensional and nonlinear slope data with outliers, improve the data quality of the model in the training phase, and predict the failed slope cases more accurately.

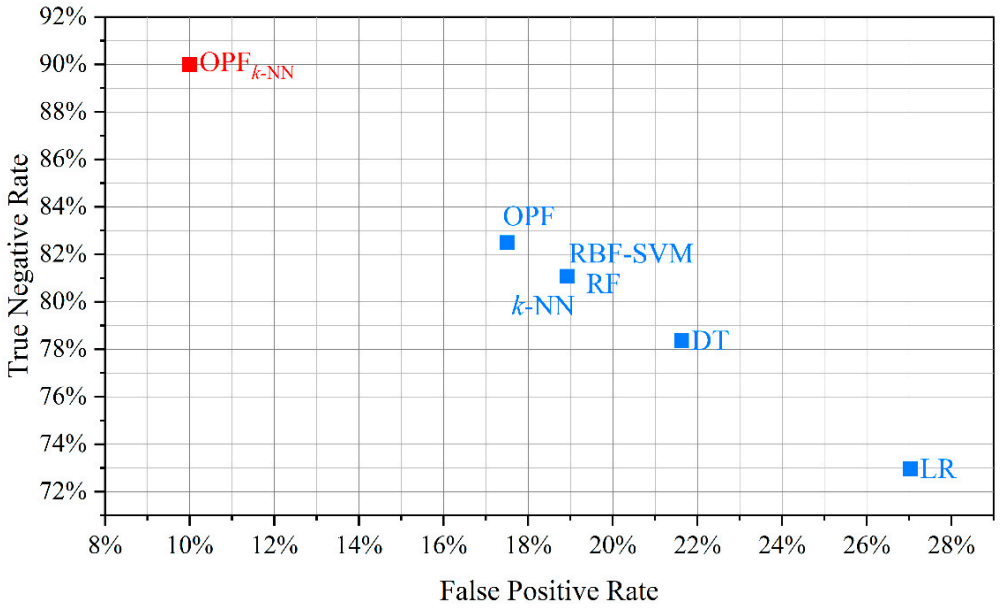

Figure 14. False positive rate and true negative rate of each classifier.

When the trade-off between AUC and the computational burden was considered, the OPF$_{k\text{-NN}}$ classifier was the most prominent because it demonstrated the optimal performance (AUC = 0.901) in less computation time (total time < 1 s) among the seven classifiers. It is worth noting that the OPF$_{k\text{-NN}}$ classifier was pretty much faster than RBF-SVM (86.2 times faster) and RF (123.1 times faster), although the difference in their performance was not significant. Therefore, the OPF$_{k\text{-NN}}$ classifier achieved the best trade-off between performance and efficiency.

According to the importance scores, all indicators were non-negligible for slope stability prediction. The physical–mechanical properties had the greatest influence on the slope stability (φ = 22%, c = 19.7%, γ = 12.3%), followed by the geometrical parameters (β = 30.5%, H = 7.93%). Some measures can be adopted to improve the slope stability from two directions. One is to optimize the slope geometry parameters, especially the slope angle. Another is to improve the physical–mechanical properties by using grouting-reinforcement techniques.

Although the OPF$_{k\text{-NN}}$ approach obtained excellent results in the slope stability prediction, there are also some limitations:

(1) More indicators should be considered. Although the six indicators in this study affect the slope stability significantly, other factors such as excavation, the properties of clay minerals, vegetation coverage, earthquake, and rainfall also have an effect on the slope stability. It is significant to analyze the influences of these indicators on the prediction results;

(2) The dataset is relatively small. The performance of ML algorithms greatly depends on the quantity and quality of data. Although the OPF$_{k\text{-NN}}$ algorithm performs well on this dataset, a better dataset might further improve the predictive performance. Therefore, it is necessary to build a larger slope database;

(3) Slopes are typically composed of multiple layers of various geotechnical materials whose properties and spatial distribution can significantly affect slope stability. As the number of slope failure cases increases, a comprehensive and diverse slope dataset should be expanded in future work. Such efforts are crucial for advancing the field of geotechnical engineering and ensuring the safety of human lives and infrastructure;

(4) The safety factor of slope stability can reflect the percentage of slope instability, and the slope stability analysis can be better considered a regression problem. Therefore, it is necessary to compile relevant data and develop relevant ML models for slope FOS value estimation in future work.

6. Engineering Application

In order to further verify the reliability of the proposed $OPF_{k\text{-}NN}$ model, it was necessary to apply it to evaluate the stability of engineering slopes. For this, eight typical slopes were collected from the Jing-xin expressway in Hebei Province, China, where landslides frequently occurred [75].

The FOS values of these eight slopes and the estimation results of the $OPF_{k\text{-}NN}$ model were recorded in Table 7. It can be seen that the overall prediction performance of the $OPF_{k\text{-}NN}$ model was consistent with the FOS values of the slopes.

Table 7. Predictive results of $OPF_{k\text{-}NN}$ model on engineering slopes.

Slopes	γ (kN/m^3)	c (kPa)	φ (°)	β (°)	H (m)	r_u	FOS	Status
1	22.4	20.0	27.0	30.0	54.0	0.12	1.208	Stable
2	21.4	31.5	42.0	34.0	18.0	0.23	2.448	Stable
3	19.0	50.0	32.0	42.0	26.0	0.17	1.786	Stable
4	19.6	17.8	29.2	41.2	50.0	0.31	0.979	Failed
5	20.2	16.7	22.3	42.4	26.6	0.47	0.869	Failed
6	20.4	25.0	20.4	35.0	65.9	0.42	0.833	Failed
7	20.0	20.0	36.0	45.0	50.0	0.14	1.102	Stable
8	23.0	18.3	25.2	39.6	61.2	0.30	0.824	Failed

7. Conclusions

Slope stability prediction is a crucial task in geotechnical engineering. This study investigated the performance of the $OPF_{k\text{-}NN}$ algorithm for the stability prediction of slopes. A total of 404 historical slope cases with failure risk from various countries were collected after considering the slope damage mechanism and geological conditions simultaneously. The $OPF_{k\text{-}NN}$, OPF, RBF-SVM, RF, k-NN, DT, and LR were used to evaluate and compare the predictive performance. To avoid the risk of overfitting or selection bias, ten-fold CV and grid search methods were selected to tune the hyperparameters. Overall, the prediction results of the $OPF_{k\text{-}NN}$ algorithm were better and more reliable, and its prediction accuracy and F_1-score were 0.901 and 0.902, respectively. According to the ROC curves and AUC values, the performance rank of the seven classifiers was $OPF_{k\text{-}NN}$ > RBF-SVM > RF > OPF > k-NN > DT > LR. In addition, the $OPF_{k\text{-}NN}$ achieved the highest TNR and the lowest FPR, which indicated that it could predict failed slope cases better. After considering the total calculation time, the $OPF_{k\text{-}NN}$ classifier achieved the optimal trade-off between performance and efficiency. Based on the importance scores of indicators, the slope angle was the most influential indicator on prediction results. Furthermore, the engineering application results showed that the overall predictive performance of the $OPF_{k\text{-}NN}$ model was consistent with the FOS value of engineering slopes.

In the future, more parameters such as excavation, the properties of clay minerals, geological formation, vegetation coverage, earthquake, and rainfall can be considered so that the feasibility of the $OPF_{k\text{-}NN}$ classifier can be further validated using more comprehensive and diverse slope datasets. In addition, the proposed methodology can be recommended for the application of other mining and geotechnical engineering projects, such as rockburst risk prediction and pillar stability prediction.

Author Contributions: Conceptualization, L.L.; methodology, L.L.; software, L.L.; validation, W.L. and G.Z.; formal analysis, L.L.; investigation, L.L.; resources, L.L.; data curation, L.L.; writing—original draft preparation, L.L.; writing—review and editing, W.L.; visualization, W.L.; supervision, G.Z.; project administration, G.Z.; funding acquisition, G.Z. and W.L. All authors have read and agreed to the published version of the manuscript.

Funding: This research was funded by the National Key Research and Development Program of China (2018YFC0604606) and the National Natural Science Foundation of China (52204117).

Data Availability Statement: The data presented in this study are available upon request from the corresponding author.

Conflicts of Interest: The authors declare no conflict of interest.

Nomenclature

Abbreviation	Full Name
AE	Acoustic emissions
LEM	Limit equilibrium method
SRM	Strength reduction method
FOS	Factor of safety
FEM	Finite element method
ML	Machine learning
RBF-SVM	Radial basis function support vector machine
DT	Decision trees
OPF	Optimum-path forest
k-NN	*k*-nearest neighbors
RF	Random forest
LR	Logistic regression
OPT	Optimal path tree
CV	Cross-validation
TP	True positive
FP	False positive
TN	True negative
FN	False negative
TNR	True negative rate
FPR	False positive rate
AUC	Area under the curve
ROC	Receiver operating characteristic

Appendix A. Database of Slope Cases

No.	Location	γ (kN/m^3)	c (kPa)	φ (°)	β (°)	H (m)	r_u	Status	Instability Type
1	Congress street, open cut slope, Chicago, USA	18.68	26.34	15	35	8.23	0	Failed	Circular
2	Brightlingsea slide, UK	16.5	11.49	0	30	3.66	0	Failed	Circular
3	Unknown	18.84	14.36	25	20	30.5	0	Stable	-
4	Unknown	18.84	57.46	20	20	30.5	0	Stable	-
5	Case 1: open pit iron ore mine, India	28.44	29.42	35	35	100	0	Stable	-
6	Case 2: open pit iron ore mine, India	28.44	39.23	38	35	100	0	Stable	-
7	Open pit chromite mine, Orissa, India	20.6	16.28	26.5	30	40	0	Failed	Circular
8	Sarukuygi landslide, Japan	14.8	0	17	20	50	0	Failed	Circular
9	Open pit iron ore mine, Goa, India	14	11.97	26	30	88	0	Failed	Circular
10	Mercoirol open pit coal mine, France	25	120	45	53	120	0	Stable	-
11	Marquesade open pit iron ore mine, Spain	26	150.05	45	50	200	0	Stable	-
12	Unknown	18.5	25	0	30	6	0	Failed	Circular
13	Unknown	18.5	12	0	30	6	0	Failed	Circular
14	Case 1: Highvale coal mine, Alberta, Canada	22.4	10	35	30	10	0	Stable	-
15	Case 2: Highvale coal mine, Alberta, Canada	21.4	10	30.34	30	20	0	Stable	-
16	Case 1: open pit coal mine, Newcastle coalfield, Australia	22	20	36	45	50	0	Failed	Circular
17	Case 2: open pit coal mine, Newcastle coalfield, Australia	22	0	36	45	50	0	Failed	Circular
18	Unknown	12	0	30	35	4	0	Stable	-

No.	Location	γ (kN/m^3)	c (kPa)	φ (°)	β (°)	H (m)	r_u	Status	Instability Type
19	Unknown	12	0	30	45	8	0	Failed	Circular
20	Pima open pit mine, Arizona, USA	23.47	0	32	37	214	0	Failed	Circular
21	Case 1: Wyoming, USA	16	70	20	40	115	0	Failed	Circular
22	Seven Sisters Landslide, UK	20.41	24.9	13	22	10.67	0.35	Stable	-
23	Case 1: The Northolt slide, UK	19.63	11.97	20	22	12.19	0.405	Failed	Circular
24	Selset Landslide, Yorkshire, UK	21.82	8.62	32	28	12.8	0.49	Failed	Circular
25	Saskatchewan dam, Canada	20.41	33.52	11	16	45.72	0.2	Failed	Circular
26	Case 2: The Northolt slide, UK	18.84	15.32	30	25	10.67	0.38	Stable	-
27	Sudbury slide, UK	18.84	0	20	20	7.62	0.45	Failed	Circular
28	Folkstone Warren slide, Kent, UK	21.43	0	20	20	61	0.5	Failed	Circular
29	River bank side, Alberta, Canada	19.06	11.71	28	35	21	0.11	Failed	Circular
30	Unknown	18.84	14.36	25	20	30.5	0.45	Failed	Circular
31	Unknown	21.51	6.94	30	31	76.81	0.38	Failed	Circular
32	Case 2: open pit iron ore mine, Goa, India	14	11.97	26	30	88	0.45	Failed	Circular
33	Athens slope, Greece	18	24	30.15	45	20	0.12	Failed	Circular
34	Open pit coal mine Allori coalfield, Italy	23	0	20	20	100	0.3	Failed	Circular
35	Case 1: open pit coal mine, Alberta, Canada	22.4	100	45	45	15	0.25	Stable	-
36	Case 2: open pit coal mine, Alberta, Canada	22.4	10	35	45	10	0.4	Failed	Circular
37	Case 3: open pit coal mine, Newcastle coalfield, Australia	20	20	36	45	50	0.25	Failed	Circular
38	Case 4: open pit coal mine, Newcastle coalfield, Australia	20	20	36	45	50	0.5	Failed	Circular
39	Case 5: open pit coal mine, Newcastle coalfield, Australia	20	0	36	45	50	0.25	Failed	Circular
40	Case 6: open pit coal mine, Newcastle coalfield, Australia	20	0	36	45	50	0.5	Failed	Circular
41	Case 1: Harbour slope, Newcastle, Australia	22	0	40	33	8	0.35	Stable	-
42	Case 2: Harbour slope, Newcastle, Australia	24	0	40	33	8	0.3	Stable	-
43	Case 3: Harbour slope, Newcastle, Australia	20	0	24.5	20	8	0.35	Stable	-
44	Case 4: Harbour slope, Newcastle, Australia	18	5	30	20	8	0.3	Stable	-
45	Unknown	27	40	35	47.1	292	0	Failed	Circular
46	Unknown	25	46	35	50	284	0	Stable	-
47	Unknown	31.3	68	37	46	366	0	Failed	Circular
48	Unknown	25	46	36	44.5	299	0	Stable	-
49	Unknown	27.3	10	39	40	480	0	Stable	-
50	Unknown	25	46	35	46	393	0	Stable	-
51	Unknown	25	48	40	49	330	0	Stable	-
52	Unknown	31.3	68.6	37	47	305	0.25	Failed	Circular
53	Unknown	25	55	36	45.5	299	0.25	Stable	-
54	Unknown	31.3	68	37	47	213	0.25	Failed	Circular
55	Three Gorges hydropower project, China	26.49	150	33	45	73	0.15	Stable	-
56	Three Gorges hydropower project, China	26.7	150	33	50	130	0.25	Stable	-
57	Three Gorges hydropower project, China	26.89	150	33	52	120	0.25	Stable	-
58	Three Gorges hydropower project, China	26.57	300	38.7	45.3	80	0.15	Failed	Unknown

No.	Location	γ (kN/m^3)	c (kPa)	φ (°)	β (°)	H (m)	r_u	Status	Instability Type
59	Three Gorges hydropower project, China	26.78	300	38.7	54	155	0.25	Failed	Unknown
60	Three Gorges hydropower project, China	26.81	200	35	58	138	0.25	Stable	Unknown
61	Three Gorges hydropower project, China	26.43	50	26.6	40	92.2	0.15	Stable	Unknown
62	Three Gorges hydropower project, China	26.69	50	26.6	50	170	0.25	Stable	Unknown
63	Three Gorges hydropower project, China	26.81	60	28.8	59	108	0.25	Stable	Unknown
64	Dingjiahe phosphorus mine, China	27.8	27.8	27	41	236	0.1	Stable	-
65	Guilin-Liuzhou highway, China	27.1	22	18.6	25.6	100	0.19	Failed	Unknown
66	Xiaolangdi reservoir, China	22.3	0	40	26.5	78	0.25	Stable	-
67	Jingzhumiao reservoir, China	18.6	0	32	26.5	46	0.25	Stable	-
68	Jingzhumiao reservoir, China	18.6	0	32	21.8	46	0.25	Stable	-
69	Yuecheng reservoir, China	18.8	9.8	21	19.29	39	0.25	Failed	Unknown
70	Yuecheng reservoir, China	21.2	0	35	18.43	73	0.25	Stable	-
71	Gushan reservoir, China	17.2	10	24.25	17.07	38	0.4	Stable	-
72	Laobu reservoir, China	19	11.9	20.4	21.04	54	0.75	Stable	-
73	Wenyuhe reservoir, China	18	5	26.5	15.52	53	0.4	Failed	Unknown
74	Wenyuhe reservoir, China	18	5	22	15.52	53	0.4	Failed	Unknown
75	Hongwuyi reservoir, China	17.4	20	24	18.43	51	0.4	Failed	Unknown
76	Hongwuyi reservoir, China	17.8	21.2	13.92	18.43	51	0.4	Stable	-
77	Lingli reservoir, China	18.8	8	26	21.8	40	0.4	Failed	Unknown
78	Lingli reservoir, China	18	21	21.33	21.8	40	0.4	Failed	Unknown
79	Zhejiang sea wall, China	17.6	10	16	21.8	9	0.4	Stable	-
80	Zhejiang sea wall, China	17.6	10	8	21.8	9	0.4	Stable	-
81	Hunan anxiang reservoir, China	17.4	14.95	21.2	45	15	0.4	Failed	Unknown
82	A reservoir dam in Jiangxi, China	18.82	25	14.6	20.32	50	0.4	Failed	Unknown
83	Qing River area landslide, China	22	29	15	18	400	0	Failed	Circular
84	Qing River area landslide, China	23	24	19.8	23	380	0	Failed	Circular
85	Qing River area landslide, China	22	40	30	30	196	0	Stable	-
86	Qing River area landslide, China	22.54	29.4	20	24	210	0	Stable	-
87	Qing River area landslide, China	22	21	23	30	257	0	Failed	Circular
88	Qing River area landslide, China	23.5	10	27	26	190	0	Failed	Circular
89	Qing River area landslide, China	22.5	18	20	20	290	0	Stable	-
90	Qing River area landslide, China	22.5	20	16	25	220	0	Stable	-
91	Qing River area landslide, China	21	20	24	21	565	0	Stable	-
92	Guzhang gaofeng slope, China	27	27.3	29.1	35	150	0.26	Failed	Circular
93	Guzhang gaofeng slope, China	27	27.3	29.1	37	184	0.22	Failed	Circular
94	Guzhang gaofeng slope, China	27	27.3	29.1	34	126.5	0.3	Failed	Circular
95	Chengmenshan open pit copper mine, China	25	46	35	50	285	0.25	Stable	-
96	Baijiagou earth slope, China	20.45	16	15	30	36	0.25	Stable	-
97	Jingping first stage hydropower station, China	27	70	22.8	45	60	0.32	Stable	-
98	Left bank accumulation body of Xiaodongjiang hydropower station, China	22	10	35	45	10	0.403	Failed	Unknown
99	Longxi landslide of Longyangxia hydropower Station, China	20	20	36	45	30	0.503	Failed	Unknown
100	Chana landslide of Longyangxia hydropower Station, China	20	0.1	36	45	50	0.25	Failed	Unknown
101	Canal slope of Baoji gorge with Wei River diversion project, China	20	0.1	36	45	50	0.503	Failed	Unknown

No.	Location	γ (kN/m^3)	c (kPa)	φ (°)	β (°)	H (m)	r_u	Status	Instability Type
102	Yellowstone landslide in the Three Gorges of the Yangtze River, China	22	0	40	33	8	0.393	Stable	-
103	Baiyian landslide in the Three Gorges reservoir area, China	24	0	40	33	8	0.303	Stable	-
104	Baihuanping landslide in the Three Gorges reservoir area, China	20	0	24.5	20	8	0.35	Stable	-
105	Gaojiazui landslide in the Three Gorges reservoir area, China	18	0	30	33	8	0.303	Stable	-
106	Songshan ancient landslide at Lechangxia hydropower station, China	27	43	35	43	420	0.25	Failed	Unknown
107	Back channel landslide in the Three Gorges reservoir area, China	27	50	40	42	407	0.25	Stable	-
108	Jipazi landslide in the Three Gorges reservoir area, China	27	35	35	42	359	0.25	Stable	-
109	Jiuxianping Landslide in the Three Gorges reservoir area, China	27	37.5	35	37.8	320	0.25	Stable	-
110	Heishe landslide, China	27	32	33	42.6	301	0.25	Failed	Unknown
111	Liujiawuchang landslide in the Three Gorges reservoir area, China	27	32	33	42.2	289	0.25	Stable	-
112	Majiaba landslide in the Three Gorges Reservoir Area, China	27.3	14	31	41	110	0.25	Stable	-
113	Sandengzi landslide in the Three Gorges Reservoir Area, China	27.3	31.5	29.703	41	135	0.25	Stable	-
114	Yaqianwan landslide in the Three Gorges Reservoir Area, China	27.3	16.8	28	50	90.5	0.25	Stable	-
115	No. 3 landslide of Sanbanxi hydropower station, China	27.3	36	1	50	92	0.25	Stable	-
116	Shijiapo landslide, China	27.3	10	39	41	511	0.25	Stable	-
117	Tanggudong landslide, China	27.3	10	39	40	470	0.25	Stable	-
118	Tianbao landslide, China	25	46	35	47	443	0.25	Stable	-
119	Shipingtai landslide of Xiaoxi hydropower station, China	25	46	35	44	435	0.25	Stable	-
120	Dongyemiao landslide, China	25	46	35	46	432	0.25	Stable	-
121	Hongtupo landslide, China	26	150	45	30	230	0.25	Failed	Unknown
122	Lianziya landslide in the Three Gorges reservoir area, China	18.5	25	0	30	6.003	0.25	Failed	Unknown
123	No. 6 landslide of Jishixia hydropower station, China	18.5	12	0	30	6.003	0.25	Failed	Unknown
124	Unknown	21.4	10	30.343	30	20	0.25	Stable	-
125	No. 1 landslide of Jishixia hydropower station, China	22	20	36	45	50	0	Failed	Unknown
126	Daxi landslide, China	22	0	36	45	50	0	Failed	Unknown
127	Right Bank landslide of Zihong reservoir, China	12	0	30	35	4	0	Stable	-
128	Zhongyangcun landslide, China	12	0	30	45	8	0	Failed	Unknown
129	Yangdagou landslide of Xunyang hydropower station, China	31.3	68	37	49	200.5	0.25	Failed	Unknown
130	Unknown	20	20	36	45	50	0.29	Failed	Unknown
131	Maidipo Landslide, China	19.6	21.8	29.5	37.8	40.3	0.25	Stable	-
132	Maidipo Landslide, China	23.1	25.2	29.2	36.5	61.9	0.4	Stable	-
133	Shaling Landslide, China	23.8	31	38.7	47.5	23.5	0.31	Stable	-
134	Niugunhan Landslide, China	22.3	20.1	31	40.2	88	0.19	Stable	-
135	Xieliupo Landslide, China	23.5	25	20	49.1	115	0.41	Stable	-
136	Zhaojiatang Landslide, China	23	20	20.3	46.2	40.3	0.25	Stable	-
137	Touzhaigou Landslide, China	21.5	15	29	41.5	123.6	0.36	Stable	-

No.	Location	γ (kN/m^3)	c (kPa)	φ (°)	β (°)	H (m)	r_u	Status	Instability Type
138	Shenzhen reservoir diversion tunnel landslide, China	23.4	15	38.5	30.3	45.2	0.28	Failed	Unknown
139	Taipingyi hydropower station diversion tunnel landslide, China	19.6	17.8	29.2	46.8	201.2	0.37	Stable	-
140	Bawangshan Landslide, China	22.1	24.2	39.7	45.8	49.5	0.21	Stable	-
141	Unknown	18.9	17.5	31	33.5	90.5	0.26	Stable	Circular
142	Unknown	20.2	16.7	22.3	42.4	26.6	0.25	Stable	Circular
143	Unknown	21.5	14	19.3	35	65.9	0.32	Stable	Circular
144	KSH Slope in Tailie elementary school, China	20	8	20	10	10	0	Failed	Unknown
145	KSH Slope on the right of Circle E of Tailie Overpass, China	27.3	37.3	31	30	30	0	Stable	-
146	KSH Landslide on the left of K71 + 625~K71 + 700, China	20.6	26.31	22	25	35	0	Failed	Unknown
147	KSH Slope of Pingxite Bridge, China	21.6	6.5	19	40	50	0	Failed	Unknown
148	KSH Slope on the right of K76 + 085~K76 + 200, China	22.4	28.9	24	28	35	0	Failed	Unknown
149	KSH Slope on the left of K77 + 920~K78 + 100, China	23.2	31.2	23	30	33	0	Failed	Unknown
150	KSH Slope on the left of K79 + 165~K79 + 300, China	26.8	37.5	32	30	26	0	Stable	-
151	KSH Slope on the right of K79 + 920~K80 + 035, China	27.4	38.1	31	25	42	0	Stable	-
152	KSH Landslide on the right of ZAK0 + 315~ZAK0 + 407, China	21.8	32.7	27	50	50	0	Failed	Unknown
153	KSH Slope on the left of K83 + 260~K83 + 360, China	21.8	27.6	25	35	60	0	Failed	Unknown
154	KSH Slope on the right of K88 + 300~K88 + 420, China	26.5	35.4	32	30	21	0	Stable	-
155	KSH Slope on the right of K88 + 700~K88 + 876, China	26.5	36.1	31	35	39	0	Stable	-
156	KSH Slope on the right of K89 + 730~K89 + 841, China	27	35.8	32	30	69	0	Stable	-
157	KSH Slope on the right of K90 + 225~K90 + 345, China	27	38.4	33	25	22	0	Stable	-
158	KSH Slope on the right of K90 + 225~K90 + 345, China	21.4	28.8	20	50	52	0	Failed	Unknown
159	KSH Slope on the left of K99 + 120~K99 + 260, China	26	42.4	37	38	55	0	Stable	-
160	KSH Slope on the left of K100 + 280~K100 + 410, China	26	39.4	36	25	30	0	Stable	-
161	KSH Slope on the left of K100 + 615~K100 + 915, China	25.6	38.8	36	25	26	0	Stable	-
162	KSH Landslide on the left of K103 + 330~K103 + 450, China	20	30.3	25	45	53	0	Failed	Unknown
163	KSH Landslide on the left of K103 + 330~K103 + 450, China	25.8	34.7	33	30	50	0	Stable	-
164	KSH Landslide on the left of K104 + 892~K105 + 052, China	21.8	28.8	26	35	99	0	Failed	Unknown
165	KSH Landslide on the left of K105 + 260~K105 + 330, China	21.8	31.2	25	30	60	0	Failed	Unknown
166	KSH Slope on the left of K106 + 268~K106 + 577, China	24	41.5	36	30	51	0	Stable	-
167	KSH Slope on the left of K106 + 992~K107 + 085, China	24	40.8	35	35	50	0	Stable	-

No.	Location	γ (kN/m^3)	c (kPa)	φ (°)	β (°)	H (m)	r_u	Status	Instability Type
168	KSH Landslide on the left of K107 + 856~K107 + 968, China	20.6	27.8	27	35	70	0	Failed	Unknown
169	KSH Landslide on the left of K108 + 960~K109 + 010, China	20.6	32.4	26	35	55	0	Failed	-
170	KSH Landslide on the left of K108 + 960~K109 + 010, China	25.8	38.2	33	27	40	0	Stable	Unknown
171	KSH Landslide on the left of K108 + 960~K109 + 010, China	25.8	39.4	33	25	45	0	Stable	Unknown
172	KSH Landslide on the left of K110 + 421~K110 + 500, China	21.1	33.5	28	40	31	0	Failed	-
173	KSH Landslide on the left of K110 + 980~K110 + 240, China	21.1	34.2	26	30	75	0	Failed	-
174	KSH Slope on the right of K112 + 720~K112 + 815, China	26.6	42.4	37	25	52	0	Stable	Unknown
175	KSH Slope on the left of K113 + 500~K113 + 580, China	26.6	44.1	38	35	42	0	Stable	Unknown
176	KSH Slope on the left of K113 + 500~K113 + 580, China	26.6	40.7	35	35	60	0	Stable	Unknown
177	KSH Slope on the left of K114 + 224~K114 + 258, China	25.8	41.2	35	30	40	0	Stable	Unknown
178	KSH Slope on the left of K117 + 200~K117 + 412, China	25.8	43.3	37	30	33	0	Stable	Unknown
179	KSH Front slope of tunnel in Songjieya K122 + 310, China	21.7	32	27	45	60	0	Failed	-
180	KSH Landslide on the right of K122 + 350~K122 + 455, China	20.6	28.5	27	40	65	0	Failed	-
181	KSH Landslide on the left of K127 + 440~K127 + 590, China	21.5	29.8	26	40	70	0	Failed	-
182	KSH Landslide on the left of K127 + 440~K127 + 590, China	26.5	42.9	38	34	36	0	Stable	Unknown
183	KSH Landslide on the left of K137 + 650~K137 + 730, China	20.8	15.6	20	30	45	0	Failed	-
184	KSH Landslide on the left of K138 + 624~K138 + 797, China	20.8	14.8	21	30	40	0	Failed	-
185	KSH Landslide on the right of K75 + 760~K76 + 000, China	19.6	29.6	23	40	58	0	Failed	-
186	KSH Slope on the right of ZBK0 + 000~ZBK0 + 185, China	25.4	33	33	20	35	0	Failed	-
187	KSH Landslide on the left of K84 + 602~K85 + 185, China	22.4	29.3	26	50	50	0	Failed	Unknown
188	KSH Slope on the right of K91 + 614~K91 + 660, China	26.2	41.5	36	35	30	0	Stable	-
189	KSH Slope on the right of K91 + 720~K91 + 771, China	26.2	42.3	36	23	36	0	Stable	-
190	KSH Slope on the left of K100 + 950~K101 + 300, China	25.6	39.8	36	30	32	0	Stable	-
191	KSH Slope on the left of K102 + 691~K102 + 880, China	25.6	36.8	34	35	60	0	Stable	-
192	KSH Slope on the right of K118 + 360~K118 + 549, China	26.2	42.8	37	30	37	0	Stable	-
193	KSH Slope on the right of K119 + 823~K119 + 951, China	26.2	43.8	38	35	68	0	Stable	-
194	KSH Landslide on the right of K124 + 340~K124 + 562, China	20.6	32.4	26	30	42	0	Failed	Unknown
195	KSH Slope on the right of K131 + 280~K131 + 380, China	26.5	41.8	36	42	54	0	Stable	-

No.	Location	γ (kN/m^3)	c (kPa)	φ (°)	β (°)	H (m)	r_u	Status	Instability Type
196	KSH Landslide on the left of K138 + 840~K138 + 930, China	20.8	15.4	21	30	53	0	Failed	Unknown
197	Unknown	17.98	4.95	30.02	19.98	8	0.3	Stable	-
198	Unknown	21.47	6.9	30.02	31.01	76.8	0.38	Failed	Circular
199	Unknown	21.78	8.55	32	27.98	12.8	0.49	Failed	Circular
200	Unknown	21.4	10	30.34	30	20	0	Stable	-
201	Unknown	21.36	10.05	30.33	30	20	0	Stable	-
202	Unknown	19.97	10.05	28.98	34.03	6	0.3	Stable	-
203	Unknown	22.38	10.05	35.01	30	10	0	Stable	-
204	Unknown	22.38	10.05	35.01	45	10	0.4	Failed	Circular
205	Unknown	19.08	10.05	9.99	25.02	50	0.4	Failed	Circular
206	Unknown	19.08	10.05	19.98	30	50	0.4	Failed	Circular
207	Unknown	18.83	10.35	21.29	34.03	37	0.3	Failed	Circular
208	Unknown	16.47	11.55	0	30	3.6	0	Failed	Circular
209	Unknown	19.03	11.7	27.99	34.98	21	0.11	Failed	Circular
210	Unknown	19.06	11.71	28	35	21	0.11	Failed	Circular
211	Unknown	19.6	12	19.98	22	12.2	0.41	Failed	Circular
212	Unknown	13.97	12	26.01	30	88	0	Failed	Circular
213	Unknown	18.46	12	0	30	6	0	Failed	Circular
214	Unknown	13.97	12	26.01	30	88	0.45	Failed	Circular
215	Unknown	18.84	14.36	25	20.3	50	0.45	Failed	Circular
216	Unknown	18.8	14.4	25.02	19.98	30.6	0	Stable	-
217	Unknown	18.8	14.4	25.02	19.98	30.6	0.45	Failed	Circular
218	Unknown	18.8	15.31	30.02	25.02	10.6	0.38	Stable	-
219	Unknown	20.56	16.21	26.51	30	40	0	Failed	Circular
220	Unknown	27.3	16.8	28	50	90.5	0.25	Stable	-
221	Unknown	27	16.8	28	50	90.5	0.25	Stable	-
222	Unknown	20.96	19.96	40.01	40.02	12	0	Stable	-
223	Unknown	21.98	19.96	36	45	50	0	Failed	Circular
224	Unknown	19.97	19.96	36	45	50	0.25	Failed	Circular
225	Unknown	19.97	19.96	36	45	50	0.5	Failed	Circular
226	Unknown	18.77	19.96	9.99	25.02	50	0.3	Failed	Circular
227	Unknown	18.77	19.96	19.98	30	50	0.3	Failed	Circular
228	Unknown	21.98	19.96	22.01	19.98	180	0.1	Failed	Circular
229	Unknown	22	20	36	45	50	0	Failed	Circular
230	Unknown	18	24	30.15	45	20	0.12	Failed	Circular
231	Unknown	18.83	24.76	21.29	29.2	37	0.5	Failed	Circular
232	Unknown	18.77	25.06	19.98	30	50	0.2	Failed	Circular
233	Unknown	18.77	25.06	9.99	25.02	50	0.2	Failed	Circular
234	Unknown	27.3	26	31	50	92	0.25	Stable	-
235	Unknown	20.96	30.01	35.01	40.02	12	0.4	Stable	-
236	Unknown	18.97	30.01	35.01	34.98	11	0.2	Stable	-
237	Unknown	27	32	33	42.4	289	0.25	Stable	-
238	Unknown	20.39	33.46	10.98	16.01	45.8	0.2	Failed	Circular
239	Unknown	20.96	34.96	27.99	40.02	12	0.5	Stable	-
240	Unknown	27	40	35	43	420	0.25	Failed	Circular
241	Unknown	19.97	40.06	30.02	30	15	0.3	Stable	-
242	Unknown	19.97	40.06	40.01	40.02	10	0.2	Stable	-
243	Unknown	20.96	45.02	25.02	49.03	12	0.3	Stable	-
244	Unknown	17.98	45.02	25.02	25.02	14	0.3	Stable	-
245	Unknown	26.7	50	26.6	50	170	0.25	Stable	-
246	Unknown	18.8	57.47	19.98	19.98	30.6	0	Stable	-
247	Unknown	26.8	60	28.8	59	108	0.25	Stable	-
248	Unknown	31.3	68	37	47	213	0.25	Failed	Circular
249	Unknown	31.3	68	37	46	366	0.25	Stable	-
250	Unknown	31.3	68.6	37	47	305	0.25	Failed	Circular

No.	Location	γ (kN/m^3)	c (kPa)	φ (°)	β (°)	H (m)	r_u	Status	Instability Type
251	Unknown	15.99	70.07	19.98	40.02	115	0	Failed	Circular
252	Unknown	22.38	99.93	45	45	15	0.25	Stable	-
253	Unknown	19.8	10	8	30	10	0.25	Stable	-
254	Unknown	19.63	11.97	20	22	21.19	0.4	Failed	Circular
255	Simulated by finite element analysis	17.93	78.2	18.49	33.42	120.79	0	Failed	Circular
256	Simulated by finite element analysis	18.02	40.92	21.18	21.86	34.65	0.1	Stable	-
257	Simulated by finite element analysis	25.76	64.11	21.4	15.76	30.38	0.5	Stable	-
258	Simulated by finite element analysis	25.55	14.8	3.44	41.06	33.31	0.4	Failed	Circular
259	Simulated by finite element analysis	23.85	78.48	33.9	22.88	118.09	0.1	Stable	-
260	Simulated by finite element analysis	18.34	92.2	40.51	40.89	139.48	0	Stable	-
261	Simulated by finite element analysis	25.15	33.36	39.25	45.48	148.37	0.3	Failed	Circular
262	Simulated by finite element analysis	19.24	65.34	34.2	21.8	64.56	0	Stable	-
263	Simulated by finite element analysis	19.91	46.83	32.8	18.15	77.25	0.2	Stable	-
264	Simulated by finite element analysis	24.36	0.41	27.04	28.44	99.28	0.3	Failed	Circular
265	Simulated by finite element analysis	20.04	67.59	42.91	25.86	4.06	0	Stable	-
266	Simulated by finite element analysis	20.31	71.43	31.46	28.18	110.81	0.2	Stable	-
267	Simulated by finite element analysis	19.26	43.88	34.26	44.16	122.49	0	Failed	Circular
268	Simulated by finite element analysis	17.99	7.2	19.23	55.56	82.75	0	Failed	Circular
269	Simulated by finite element analysis	17.85	73.21	22.22	46.32	77.08	0	Failed	Circular
270	Simulated by finite element analysis	19.14	94.52	14.6	33.78	105.01	0.5	Failed	Circular
271	Simulated by finite element analysis	21.01	44.08	26.49	28.94	97.57	0	Failed	Circular
272	Simulated by finite element analysis	19.33	99.3	33.1	34.82	55.54	0	Stable	-
273	Simulated by finite element analysis	16.1	65.25	20.21	20.17	17.27	0.3	Stable	-
274	Simulated by finite element analysis	19.9	73.05	45.46	32.99	9.53	0.4	Stable	-
275	Simulated by finite element analysis	19.62	3.67	31.06	5.87	92.13	0.4	Stable	-
276	Simulated by finite element analysis	20.71	28.37	14.49	26.49	63.78	0	Failed	Circular
277	Simulated by finite element analysis	22.12	37.55	38.11	33.33	29.93	0.1	Stable	-
278	Simulated by finite element analysis	21.54	32.07	18.89	27.06	58.89	0.3	Failed	Circular
279	Simulated by finite element analysis	17.4	108.19	30.04	47.3	111.28	0.3	Failed	Circular
280	Simulated by finite element analysis	17.39	20.26	26.6	56.38	34.45	0.3	Failed	Circular
281	Simulated by finite element analysis	18.63	106.66	14.27	38.62	68.73	0.5	Failed	Circular
282	Simulated by finite element analysis	17.68	94.92	25.4	45.11	65.97	0.4	Failed	Circular
283	Simulated by finite element analysis	14.59	10.92	27.55	47.11	141.66	0.1	Failed	Circular
284	Simulated by finite element analysis	18.72	87.53	23.28	33.15	61.82	0	Stable	-
285	Simulated by finite element analysis	15.17	35.57	42.06	14.6	183.27	0	Stable	-
286	Simulated by finite element analysis	15.79	31.63	28.09	48.97	12.09	0.5	Stable	-
287	Simulated by finite element analysis	15.87	69.53	48.47	27.1	17.83	0	Stable	-
288	Simulated by finite element analysis	16.56	74.15	18.33	37.2	31.92	0	Stable	-
289	Simulated by finite element analysis	16.27	44.32	21.6	27.07	151.39	0.4	Failed	Circular
290	Simulated by finite element analysis	17.09	52.7	26	42.55	17.87	0.4	Stable	-
291	Simulated by finite element analysis	19.49	100.82	31.34	54.81	21.06	0.3	Stable	-
292	Simulated by finite element analysis	23.46	56.15	31.06	43.67	53.54	0	Failed	Circular
293	Simulated by finite element analysis	15.48	46.54	43.56	39.42	14.92	0.2	Stable	-
294	Simulated by finite element analysis	24.36	64.7	39.14	46.87	141.85	0.3	Failed	Circular
295	Simulated by finite element analysis	22.39	59.91	11.89	22.7	94.67	0.2	Failed	Circular
296	Simulated by finite element analysis	22.42	161.55	20.7	39.03	15.89	0	Stable	-
297	Simulated by finite element analysis	19.51	63.27	37.01	18.77	90.45	0.4	Stable	-
298	Simulated by finite element analysis	21.16	124	21.92	30.41	116.84	0.5	Stable	-
299	Simulated by finite element analysis	22.53	34.61	26.81	58	102.93	0	Failed	Circular
300	Simulated by finite element analysis	22.77	27.51	25.23	14.95	67.59	0.2	Stable	-
301	Simulated by finite element analysis	19.2	55.28	24.02	29.8	91.59	0.3	Failed	Circular
302	Simulated by finite element analysis	23.17	17.75	23.6	53.51	24.8	0.3	Failed	Circular
303	Simulated by finite element analysis	24.89	121.63	30.2	35.32	16.18	0.5	Stable	-
304	Simulated by finite element analysis	24.03	72.37	28.77	37.74	59.21	0.1	Stable	-
305	Simulated by finite element analysis	23.05	12.16	14	23.3	89.05	0	Failed	Circular
306	Simulated by finite element analysis	18.22	77.64	46.58	43.19	24.52	0.4	Stable	-

No.	Location	γ (kN/m^3)	c (kPa)	φ (°)	β (°)	H (m)	r_u	Status	Instability Type
307	Simulated by finite element analysis	20.47	16.87	35.48	27.58	17.86	0	Stable	-
308	Simulated by finite element analysis	20.99	63.58	48.54	30.91	68.82	0	Stable	-
309	Simulated by finite element analysis	18.74	49.05	17.54	14.34	118.98	0	Failed	Circular
310	Simulated by finite element analysis	21.26	9.78	43.23	17.42	90.73	0	Stable	-
311	Simulated by finite element analysis	21.07	29.89	14.46	21.98	22.31	0	Failed	Circular
312	Simulated by finite element analysis	20.27	25.33	23.75	8.37	42.76	0	Stable	-
313	Simulated by finite element analysis	19.9	25.05	25.46	44.15	37.03	0	Failed	Circular
314	Simulated by finite element analysis	20.32	14.9	14.35	42.66	80.26	0	Failed	Circular
315	Simulated by finite element analysis	20.57	34.55	44.41	38.36	122.28	0	Stable	-
316	Simulated by finite element analysis	19.1	133.38	41.5	31.38	109.11	0	Stable	-
317	Simulated by finite element analysis	18.88	9.77	21.01	51.49	33.34	0	Failed	Circular
318	Simulated by finite element analysis	20.26	122.61	23.44	24.92	114.17	0	Stable	-
319	Simulated by finite element analysis	16.3	91.72	27.7	41.82	87.53	0	Failed	Circular
320	Simulated by finite element analysis	13.6	58.07	38.63	36.61	32.97	0	Stable	-
321	Simulated by finite element analysis	19.65	28.79	17.38	35.79	68.78	0	Failed	Circular
322	Simulated by finite element analysis	16.1	81.18	30.16	4.84	125.44	0	Stable	-
323	Simulated by finite element analysis	26.52	68.74	20.76	24.86	123.99	0	Failed	Circular
324	Simulated by finite element analysis	23.12	57.21	29.96	26.39	94.95	0	Stable	-
325	Simulated by finite element analysis	25.06	14.97	14.86	47.79	142.71	0	Failed	Circular
326	Simulated by finite element analysis	23.15	46.41	23.56	48.54	22.44	0	Failed	Circular
327	Simulated by finite element analysis	19.27	129.46	27.54	34.61	87.63	0	Stable	-
328	Simulated by finite element analysis	22.3	40.64	21.93	24.05	103.19	0	Failed	Circular
329	Simulated by finite element analysis	22.37	43.37	19.15	45.03	119.95	0	Failed	Circular
330	Simulated by finite element analysis	15.37	53.03	28.06	40.94	79	0.35	Failed	Circular
331	Simulated by finite element analysis	23.35	29.97	16.38	39.73	33.92	0.405	Failed	Circular
332	Simulated by finite element analysis	17.14	127.05	41.92	31.87	114.99	0.49	Stable	-
333	Simulated by finite element analysis	16.1	71.69	20.81	52.77	70.06	0.2	Failed	Circular
334	Simulated by finite element analysis	23.18	17.74	13.86	26.71	60.39	0.38	Failed	Circular
335	Simulated by finite element analysis	18.34	36.34	30.19	29.44	143.1	0.45	Failed	Circular
336	Simulated by finite element analysis	16.9	31.8	33.65	29.21	81.74	0.5	Stable	-
337	Simulated by finite element analysis	24.83	119.28	13.24	26.86	113.91	0.11	Failed	Circular
338	Simulated by finite element analysis	13.93	80.9	37.13	34.16	58.25	0.45	Stable	-
339	Simulated by finite element analysis	17.61	59.31	19.1	43.28	31.25	0.38	Failed	Circular
340	Simulated by finite element analysis	24.6	11.36	1.7	20.19	11.06	0.45	Failed	Circular
341	Simulated by finite element analysis	30.31	22	23.94	36.99	104.02	0.12	Failed	Circular
342	Simulated by finite element analysis	20.69	69.68	40.34	49.39	111.42	0.3	Failed	Circular
343	Simulated by finite element analysis	23.82	300	21.77	20.57	23.9	0.25	Stable	-
344	Simulated by finite element analysis	16.77	24.09	34	22.53	26.72	0.4	Stable	-
345	Simulated by finite element analysis	28.11	0.69	21	18.22	99.46	0.25	Failed	Circular
346	Simulated by finite element analysis	18.27	6.45	20.69	26.3	17.04	0.5	Failed	Circular
347	Simulated by finite element analysis	10.06	62.41	39.99	39.04	58.31	0.25	Stable	-
348	Simulated by finite element analysis	20.85	74.42	11.34	39.57	13.17	0.5	Stable	-
349	Simulated by finite element analysis	20.98	52.5	23.55	33.67	49.7	0.35	Failed	Circular
350	Simulated by finite element analysis	17.56	27.82	17.23	37.23	67.61	0.3	Failed	Circular
351	Simulated by finite element analysis	21.4	67.99	38.11	32.72	132.33	0.35	Stable	-
352	Simulated by finite element analysis	25.29	125.82	0	48.07	56	0.3	Stable	-
353	Simulated by finite element analysis	15.47	79.39	47.88	32.46	81.14	0.15	Stable	-
354	Simulated by finite element analysis	22.3	38.64	31.01	43.92	47	0.25	Failed	Circular
355	Simulated by finite element analysis	16.82	0.05	23.92	29.45	36.22	0.25	Failed	Circular
356	Simulated by finite element analysis	25.93	13.72	22.36	35.79	53.37	0.15	Stable	-
357	Simulated by finite element analysis	22.56	63.51	31.13	38.36	49.54	0.25	Stable	-
358	Simulated by finite element analysis	18.56	21.04	24.82	5.3	45.92	0.25	Stable	-
359	Simulated by finite element analysis	21.47	41.59	18.76	45.73	48.47	0.15	Failed	Circular
360	Simulated by finite element analysis	19.01	29.34	12.19	30.35	12.07	0.25	Stable	-
361	Simulated by finite element analysis	22.84	68.46	10.91	35.94	63.73	0.25	Failed	Circular
362	Simulated by finite element analysis	20.36	11.89	36.6	16.58	108.92	0	Stable	-

No.	Location	γ (kN/m^3)	c (kPa)	φ (°)	β (°)	H (m)	r_u	Status	Instability Type
363	Simulated by finite element analysis	25.28	83.67	18.4	36.46	106.8	0.1	Failed	Circular
364	Simulated by finite element analysis	30.27	38.55	22.46	39	29.53	0.5	Failed	Circular
365	Simulated by finite element analysis	21.71	16.57	19.68	29	60.8	0.4	Failed	Circular
366	Simulated by finite element analysis	23.67	55.72	38.36	38.68	100.02	0.1	Stable	-
367	Simulated by finite element analysis	21.84	53.21	35.12	15.3	108.67	0	Stable	-
368	Simulated by finite element analysis	18.58	82.65	21.89	31.64	20.11	0.3	Stable	-
369	Simulated by finite element analysis	22.23	30.81	21.8	31.44	3.45	0	Stable	-
370	Simulated by finite element analysis	24.05	30.89	28.57	36.87	71.36	0.2	Failed	Circular
371	Simulated by finite element analysis	23.57	162.62	12.59	56.79	155.28	0.3	Failed	Circular
372	Simulated by finite element analysis	21.03	8.32	28.22	31.63	49.25	0	Failed	Circular
373	Simulated by finite element analysis	19.88	30.86	21.47	50.14	38.23	0.2	Failed	Circular
374	Simulated by finite element analysis	27.2	53.62	28.3	21.82	56.78	0	Stable	-
375	Simulated by finite element analysis	23.88	43.5	26.48	43.07	13.52	0	Stable	-
376	Simulated by finite element analysis	25.55	64.91	16.97	33.45	97.58	0	Failed	Circular
377	Simulated by finite element analysis	18.04	38.49	43.96	32.44	27.54	0.5	Stable	-
378	Simulated by finite element analysis	25.7	84.49	18.66	42.65	7.75	0	Stable	-
379	Simulated by finite element analysis	15.07	3.58	35.12	36.52	22.1	0	Failed	Circular
380	Simulated by finite element analysis	22.21	86.74	27.43	25.2	13.37	0.3	Stable	-
381	Simulated by finite element analysis	20.56	46.9	13.47	10.75	3.88	0.4	Stable	-
382	Simulated by finite element analysis	21.05	95.94	36.24	37.34	132.92	0.4	Stable	-
383	Simulated by finite element analysis	18.93	9.28	31.46	43.31	33.06	0	Failed	Circular
384	Simulated by finite element analysis	23.88	10.07	22.75	28.3	23.92	0.1	Failed	Circular
385	Simulated by finite element analysis	22.44	10.48	31.88	26.22	101.93	0.3	Stable	-
386	Simulated by finite element analysis	21.17	12.58	40.51	49.4	111.54	0.3	Failed	Circular
387	Simulated by finite element analysis	28.07	160.77	26.2	24.64	162.76	0.3	Stable	-
388	Simulated by finite element analysis	24.3	45.96	44.35	38.12	56.21	0.5	Stable	-
389	Simulated by finite element analysis	21.13	76.34	37.55	19.9	5.05	0.4	Stable	-
390	Simulated by finite element analysis	20.41	44.66	28.23	33.89	86.39	0.1	Failed	Circular
391	Simulated by finite element analysis	13.12	94.38	8.11	20.66	34.42	0	Stable	-
392	Simulated by finite element analysis	18.09	11.87	3.46	34.43	78.52	0	Failed	Circular
393	Simulated by finite element analysis	18.67	115.4	27.1	14.56	91.16	0.5	Stable	-
394	Simulated by finite element analysis	17.46	99.03	24.1	4.24	42.94	0	Stable	-
395	Simulated by finite element analysis	20.05	91.29	32.17	39.26	70.97	0	Stable	-
396	Simulated by finite element analysis	27.17	14.55	15.02	44.82	19.18	0.4	Failed	Circular
397	Simulated by finite element analysis	22.35	0	57.36	37.5	15.1	0.4	Stable	-
398	Simulated by finite element analysis	19.58	0	14.6	27.18	77.83	0.3	Failed	Circular
399	Simulated by finite element analysis	16.44	0	29.22	40.24	21.74	0	Stable	-
400	Simulated by finite element analysis	23.96	0	28.04	32.4	74.58	0.2	Failed	Circular
401	Simulated by finite element analysis	19.6	0	22.79	59.35	155.73	0.3	Failed	Circular
402	Simulated by finite element analysis	27.35	0	33.92	34.03	5.7	0.2	Failed	Circular
403	Simulated by finite element analysis	21.03	0	17.72	5.79	57.31	0	Stable	-
404	Simulated by finite element analysis	25.74	0	17.23	30.03	80.53	0.4	Failed	Circular

Case 1–44 reported by [32]. Case 45–54 reported by [63]. Case 55–63 reported by [64]. Case 64 reported by [65]. Case 65–82 reported by [70]. Case 83–91 reported by [66]. Case 92–94 reported by [67]. Case 95–97 reported by [36]. Case 98–140 reported by [68]. Case 141–143 reported by [36]. Case 144–196 reported by [72]. Case 197–254 reported by [69]. Case 255–404 reported by [57]. KSH denotes Kaili-Sansui highway.

References

1. Zhan, L.-T.; Guo, X.-G.; Sun, Q.-Q.; Chen, Y.-M.; Chen, Z.-Y. The 2015 Shenzhen catastrophic landslide in a construction waste dump: Analyses of undrained strength and slope stability. *Acta Geotech.* **2021**, *16*, 1247–1263. [CrossRef]
2. Asnakew, S.; Shumet, S.; Ginbare, W.; Legas, G.; Haile, K. Prevalence of post-traumatic stress disorder and associated factors among Koshe landslide survivors, Addis Ababa, Ethiopia: A community-based, cross-sectional study. *BMJ Open* **2019**, *9*, e028550. [CrossRef] [PubMed]
3. Van Tien, P.; Luong, L.H.; Duc, D.M.; Trinh, P.T.; Quynh, D.T.; Lan, N.C.; Thuy, D.T.; Phi, N.Q.; Cuong, T.Q.; Dang, K.; et al. Rainfall-induced catastrophic landslide in Quang Tri Province: The deadliest single landslide event in Vietnam in 2020. *Landslides* **2021**, *18*, 2323–2327. [CrossRef]

4. Zhang, C.-C.; Zhu, H.-H.; Liu, S.-P.; Shi, B.; Zhang, D. A kinematic method for calculating shear displacements of landslides using distributed fiber optic strain measurements. *Eng. Geol.* **2018**, *234*, 83–96. [CrossRef]
5. Dixon, N.; Smith, A.; Flint, J.A.; Khanna, R.; Clark, B.; Andjelkovic, M. An acoustic emission landslide early warning system for communities in low-income and middle-income countries. *Landslides* **2018**, *15*, 1631–1644. [CrossRef]
6. Shiotani, T. Evaluation of long-term stability for rock slope by means of acoustic emission technique. *NDT E Int.* **2006**, *39*, 217–228. [CrossRef]
7. Codeglia, D.; Dixon, N.; Fowmes, G.J.; Marcato, G. Analysis of acoustic emission patterns for monitoring of rock slope deformation mechanisms. *Eng. Geol.* **2017**, *219*, 21–31. [CrossRef]
8. Akbar, T.A.; Ha, S.R. Landslide hazard zoning along Himalayan Kaghan Valley of Pakistan—By integration of GPS, GIS, and remote sensing technology. *Landslides* **2011**, *8*, 527–540. [CrossRef]
9. Marsella, M.; D'Aranno, P.J.V.; Scifoni, S.; Sonnessa, A.; Corsetti, M. Terrestrial laser scanning survey in support of unstable slopes analysis: The case of Vulcano Island (Italy). *Nat. Hazard.* **2015**, *78*, 443–459. [CrossRef]
10. Atzeni, C.; Barla, M.; Pieraccini, M.; Antolini, F. Early Warning Monitoring of Natural and Engineered Slopes with Ground-Based Synthetic-Aperture Radar. *Rock Mech Rock Eng.* **2015**, *48*, 235–246. [CrossRef]
11. Ho, S.-C.; Chen, I.H.; Lin, Y.-S.; Chen, J.-Y.; Su, M.-B. Slope deformation monitoring in the Jiufenershan landslide using time domain reflectometry technology. *Landslides* **2019**, *16*, 1141–1151. [CrossRef]
12. Chen, Z.Y.; Mi, H.L.; Zhang, F.M.; Wang, X.G. A simplified method for 3D slope stability analysis. *Can. Geotech. J.* **2003**, *40*, 675–683. [CrossRef]
13. Nie, Z.; Zhang, Z.; Zheng, H. Slope stability analysis using convergent strength reduction method. *Eng. Anal. Boundary Elem.* **2019**, *108*, 402–410. [CrossRef]
14. Wang, L.; Sun, D.; Li, L. Three-dimensional stability of compound slope using limit analysis method. *Can. Geotech. J.* **2019**, *56*, 116–125. [CrossRef]
15. Liu, H.; Xu, D.; Min, Y. Discussion on the Multi-Solution of Three-Dimensional Slope Safety Factor. *Geotech. Geol. Eng.* **2021**, *39*, 3361–3370. [CrossRef]
16. Faramarzi, L.; Zare, M.; Azhari, A.; Tabaei, M. Assessment of rock slope stability at Cham-Shir Dam Power Plant pit using the limit equilibrium method and numerical modeling. *Bull. Eng. Geol. Environ.* **2017**, *76*, 783–794. [CrossRef]
17. Liu, F. Stability Analysis of Geotechnical Slope Based on Strength Reduction Method. *Geotech. Geol. Eng.* **2020**, *38*, 3653–3665. [CrossRef]
18. Mbarka, S.; Baroth, J.; Ltifi, M.; Hassis, H.; Darve, F. Reliability analyses of slope stability. *Eur. J. Environ. Civ. Eng.* **2010**, *14*, 1227–1257. [CrossRef]
19. Ma, Z.; Liao, H.; Dang, F.; Cheng, Y. Seismic slope stability and failure process analysis using explicit finite element method. *Bull. Eng. Geol. Environ.* **2021**, *80*, 1287–1301. [CrossRef]
20. Nie, Z.; Zhang, Z.; Zheng, H.; Lin, S. Stability analysis of landslides using BEM and variational inequality based contact model. *Comput. Geotech.* **2020**, *123*, 103575. [CrossRef]
21. Zhao, Y.; Zhao, G.; Zhou, J.; Ma, J.; Cai, X. Failure mechanism analysis of rock in particle discrete element method simulation based on moment tensors. *Comput. Geotech.* **2021**, *136*, 104215. [CrossRef]
22. Yang, Y.; Xu, D.; Liu, F.; Zheng, H. Modeling the entire progressive failure process of rock slopes using a strength-based criterion. *Comput. Geotech.* **2020**, *126*, 103726. [CrossRef]
23. Sun, L.; Grasselli, G.; Liu, Q.; Tang, X.; Abdelaziz, A. The role of discontinuities in rock slope stability: Insights from a combined finite-discrete element simulation. *Comput. Geotech.* **2022**, *147*, 104788. [CrossRef]
24. Ma, Z.; Zhu, C.; Yao, X.; Dang, F. Slope Stability Analysis under Complex Stress State with Saturated and Unsaturated Seepage Flow. *Geofluids* **2021**, *2021*, 6637098. [CrossRef]
25. Wei, J.; Zhao, Z.; Xu, C.; Wen, Q. Numerical investigation of landslide kinetics for the recent Mabian landslide (Sichuan, China). *Landslides* **2019**, *16*, 2287–2298. [CrossRef]
26. Haghnejad, A.; Ahangari, K.; Moarefvand, P.; Goshtasbi, K. Numerical investigation of the impact of geological discontinuities on the propagation of ground vibrations. *Geomech. Eng.* **2018**, *14*, 545–552. [CrossRef]
27. Song, X.; Zhang, X.; Wu, S. Study on slope stability analysis and large deformation characteristics of failure based on SPH method. *Comput. Part. Mech.* **2023**. [CrossRef]
28. Zhang, Y.W.; Tang, L.X.; Bai, D.C.; Zhou, P. Numerical Simulation of Failure Process on Soil Slope with Different Support Measures. *Appl. Mech. Mater.* **2014**, *580–583*, 665–668. [CrossRef]
29. Dyson, A.P.; Tolooiyan, A. Comparative Approaches to Probabilistic Finite Element Methods for Slope Stability Analysis. *Simul. Modell Pract. Theory* **2020**, *100*, 102061. [CrossRef]
30. Liang, W.; Luo, S.; Zhao, G.; Wu, H. Predicting Hard Rock Pillar Stability Using GBDT, XGBoost, and LightGBM Algorithms. *Mathematics* **2020**, *8*, 765. [CrossRef]
31. Lu, P.; Rosenbaum, M.S. Artificial neural networks and Grey Systems for the prediction of slope stability. *Nat. Hazard.* **2003**, *30*, 383–398. [CrossRef]
32. Sah, N.K.; Sheorey, P.R.; Upadhyaya, L.N. Maximum likelihood estimation of slope stability. *Int. J. Rock Mech. Mining Sci. Geomech. Abstracts* **1994**, *31*, 47–53. [CrossRef]
33. Samui, P. Slope stability analysis: A support vector machine approach. *Environ. Geol.* **2008**, *56*, 255–267. [CrossRef]

34. Yang, C.X.; Tham, L.G.; Feng, X.T.; Wang, Y.J.; Lee, P.K.K. Two-stepped evolutionary algorithm and its application to stability analysis of slopes. *J. Comput. Civ. Eng.* **2004**, *18*, 145–153. [CrossRef]
35. Amirkiyaei, V.; Ghasemi, E. Stability assessment of slopes subjected to circular-type failure using tree-based models. *Int. J. Geotech. Eng.* **2020**, *16*, 301–311. [CrossRef]
36. Zhou, J.; Li, E.; Yang, S.; Wang, M.; Shi, X.; Yao, S.; Mitri, H.S. Slope stability prediction for circular mode failure using gradient boosting machine approach based on an updated database of case histories. *Saf. Sci.* **2019**, *118*, 505–518. [CrossRef]
37. Wang, H.; Moayedi, H.; Kok Foong, L. Genetic algorithm hybridized with multilayer perceptron to have an economical slope stability design. *Eng. Comput.* **2021**, *37*, 3067–3078. [CrossRef]
38. Hoang, N.-D.; Tien Bui, D. Chapter 18—Slope Stability Evaluation Using Radial Basis Function Neural Network, Least Squares Support Vector Machines, and Extreme Learning Machine. In *Handbook of Neural Computation*; Samui, P., Sekhar, S., Balas, V.E., Eds.; Academic Press: Cambridge, MA, USA, 2017; pp. 333–344.
39. Mahmoodzadeh, A.; Mohammadi, M.; Ali, H.F.H.; Ibrahim, H.H.; Abdulhamid, S.N.; Nejati, H.R. Prediction of safety factors for slope stability: Comparison of machine learning techniques. *Nat. Hazard.* **2021**, *111*, 1771–1799. [CrossRef]
40. Papa, J.P.; Falcao, A.X.; Levada, A.L.; Corrêa, D.C.; Salvadeo, D.H.; Mascarenhas, N.D. Fast and accurate holistic face recognition using optimum-path forest. In Proceedings of the 2009 16th International Conference on Digital Signal Processing, Santorini, Greece, 5–7 July 2009; pp. 1–6.
41. Bernardo, L.S.; Quezada, A.; Munoz, R.; Maia, F.M.; Pereira, C.R.; Wu, W.; de Albuquerque, V.H.C. Handwritten pattern recognition for early Parkinson's disease diagnosis. *Pattern Recognit Lett.* **2019**, *125*, 78–84. [CrossRef]
42. Papa, J.P.; Spadotto, A.A.; Falcao, A.X.; Pereira, J.C. Optimum path forest classifier applied to laryngeal pathology detection. In Proceedings of the 2008 15th International Conference on Systems, Signals and Image Processing, Bratislava, Slovakia, 25–28 June 2008; pp. 249–252.
43. Pisani, R.J.; Mizobe Nakamura, R.Y.; Riedel, P.S.; Lopes Zimback, C.R.; Falcao, A.X.; Papa, J.P. Toward Satellite-Based Land Cover Classification Through Optimum-Path Forest. *IEEE Trans Geosci. Remote Sens.* **2014**, *52*, 6075–6085. [CrossRef]
44. Bertoni, M.A.; de Rosa, G.H.; Brega, J.R.F. Optimum-path forest stacking-based ensemble for intrusion detection. *Evol. Intell.* **2021**, *15*, 2037–2054. [CrossRef]
45. Papa, J.P.; Nachif Fernandes, S.E.; Falcao, A.X. Optimum-Path Forest based on k-connectivity: Theory and applications. *Pattern Recognit Lett.* **2017**, *87*, 117–126. [CrossRef]
46. Hensel, F.; Moor, M.; Rieck, B. A Survey of Topological Machine Learning Methods. *Front. Artif. Intell.* **2021**, *4*, 681108. [CrossRef]
47. Papa, J.P.; Falcao, A.X.; Suzuki, C.T.N. Supervised Pattern Classification Based on Optimum-Path Forest. *Int. J. Imaging Syst. Technol.* **2009**, *19*, 120–131. [CrossRef]
48. Papa, J.P.; Falcao, A.X.; de Albuquerque, V.H.C.; Tavares, J.M.R.S. Efficient supervised optimum-path forest classification for large datasets. *Pattern Recognit.* **2012**, *45*, 512–520. [CrossRef]
49. Chen, S.; Sun, T.; Yang, F.; Sun, H.; Guan, Y. An improved optimum-path forest clustering algorithm for remote sensing image segmentation. *Comput. Geosci.* **2018**, *112*, 38–46. [CrossRef]
50. Papa, J.P.; Falcao, A.X. A New Variant of the Optimum-Path Forest Classifier. In Proceedings of the 4th International Symposium on Visual Computing, Las Vegas, NV, USA, 16–18 October 2008; pp. 935–944.
51. Zhao, G.; Wang, M.; Liang, W. A Comparative Study of SSA-BPNN, SSA-ENN, and SSA-SVR Models for Predicting the Thickness of an Excavation Damaged Zone around the Roadway in Rock. *Mathematics* **2022**, *10*, 1351. [CrossRef]
52. Liang, W.; Sari, A.; Zhao, G.; McKinnon, S.D.; Wu, H. Short-term rockburst risk prediction using ensemble learning methods. *Nat. Hazard.* **2020**, *104*, 1923–1946. [CrossRef]
53. de Rosa, G.H.; Papa, J.P. OPFython: A Python implementation for Optimum-Path Forest. *Software Impacts* **2021**, *9*, 100113. [CrossRef]
54. Pedregosa, F.; Varoquaux, G.; Gramfort, A.; Michel, V.; Thirion, B.; Grisel, O.; Blondel, M.; Prettenhofer, P.; Weiss, R.; Dubourg, V.; et al. Scikit-learn: Machine Learning in Python. *J. Mach. Learn Res.* **2011**, *12*, 2825–2830.
55. Yuan, C.; Moayedi, H. The performance of six neural-evolutionary classification techniques combined with multi-layer perception in two-layered cohesive slope stability analysis and failure recognition. *Eng. Comput.* **2020**, *36*, 1705–1714. [CrossRef]
56. Bradley, A.P. The use of the area under the ROC curve in the evaluation of machine learning algorithms. *Pattern Recognit.* **1997**, *30*, 1145–1159. [CrossRef]
57. Kardani, N.; Zhou, A.; Nazem, M.; Shen, S.-L. Improved prediction of slope stability using a hybrid stacking ensemble method based on finite element analysis and field data. *J. Rock Mech. Geotech. Eng.* **2021**, *13*, 188–201. [CrossRef]
58. Moayedi, H.; Osouli, A.; Nguyen, H.; Rashid, A.S.A. A novel Harris hawks' optimization and k-fold cross-validation predicting slope stability. *Eng. Comput.* **2021**, *37*, 369–379. [CrossRef]
59. Liang, W.; Sari, Y.A.; Zhao, G.; McKinnon, S.D.; Wu, H. Probability Estimates of Short-Term Rockburst Risk with Ensemble Classifiers. *Rock Mech Rock Eng.* **2021**, *54*, 1799–1814. [CrossRef]
60. Bishop, A.W.; Morgenstern, N. Stability Coefficients for Earth Slopes. *Geotechnique* **1960**, *10*, 129–153. [CrossRef]
61. Fellenius, W. Calculation of stability of Earth dam. In *Transactions of the Second Congress Large Dams*; International Commission on Large Dams: Washington, DC, USA, 1936; pp. 445–462.
62. Morgenstern, N.R.; Price, V.E. The Analysis of the Stability of General Slip Surfaces. *Geotechnique* **1965**, *15*, 79–93. [CrossRef]

63. Feng, X.-T.; Hudson, J.A. The ways ahead for rock engineering design methodologies. *Int. J. Rock Mech. Min. Sci.* **2004**, *41*, 255–273. [CrossRef]
64. Xu, W.; Shao, J.F. Artificial Neural Network Analysis for the Evaluation of Slope Stability. In *Application of Numerical Methods to Geotechnical Problems*; Cividini, A., Ed.; Springer: Vienna, Austria, 1998; pp. 665–672.
65. Li, W.-X.; Yang, S.-C.; Chen, E.-Z.; Qiao, J.-L.; Dai, L.-F. Neural network method of analysis of natural slope failure due to underground mining in mountainous areas. *Yantu Lixue Rock Soil Mech.* **2006**, *27*, 1563–1566.
66. Wang, H.B.; Xu, W.Y.; Xu, R.C. Slope stability evaluation using back propagation neural networks. *Eng. Geol.* **2005**, *80*, 302–315. [CrossRef]
67. Jin, L.; Feng, W.; Zhang, J. Maximum likelihood estimation on safety coefficients of rocky slope near DAM of Fengtan project. *Yanshilixue Yu Gongcheng Xuebao/Chinese J. Rock Mech. Eng.* **2004**, *23*, 1891–1894.
68. Wang, C. Study on Prediction Methods for High Engineering Slope. Master's Thesis, Beijing Jiaotong University, Beijing, China, 2009.
69. Qi, C.; Tang, X. Slope stability prediction using integrated metaheuristic and machine learning approaches: A comparative study. *Comput. Ind. Eng.* **2018**, *118*, 112–122. [CrossRef]
70. Chen, L.-Q.; Peng, Z.-B.; Chen, W.; Peng, W.-X.; Wu, Q.-H. Artificial neural network simulation on prediction of clay slope stability based on fuzzy controller. *Zhongnan Daxue Xuebao Ziran Kexue Ban J. Central South Univ. Sci. Technol.* **2009**, *40*, 1381–1387.
71. Lin, S.; Zheng, H.; Han, B.; Li, Y.; Han, C.; Li, W. Comparative performance of eight ensemble learning approaches for the development of models of slope stability prediction. *Acta Geotech.* **2022**, *17*, 1477–1502. [CrossRef]
72. Chen, C.; Xiao, Z.; Zhang, G. Stability assessment model for epimetamorphic rock slopes based on adaptive neuro-fuzzy inference system. *Electron. J. Geotech. Eng.* **2011**, *16 A*, 93–107.
73. Altmann, A.; Tolosi, L.; Sander, O.; Lengauer, T.J.B. Permutation importance: A corrected feature importance measure. *Bioinformatics* **2010**, *26*, 1340–1347. [CrossRef] [PubMed]
74. Viet-Ha, N.; Nhat-Duc, H.; Hieu, N.; Phuong Thao Thi, N.; Tinh Thanh, B.; Pham Viet, H.; Samui, P.; Dieu Tien, B. Effectiveness assessment of Keras based deep learning with different robust optimization algorithms for shallow landslide susceptibility mapping at tropical area. *Catena* **2020**, *188*, 104458. [CrossRef]
75. Sun Jishu, X.J.; Wang, J.; Li, W. Application of Relevance Vector Machine Model in Slope Stability Prediction. *Sci. Tech. Eng.* **2021**, *21*, 12234–12242.